Chapter 7
Arc Welding and Hybrid Laser-Arc Welding

Ian Richardson

Abstract Laser-arc hybrid welding has developed into a viable industrial technology in recent years with a number of technological applications. The physics of the underlying interactions between the laser beam and arc plasma is quite complex and, in order to explore the relationships involved, it is useful first to consider important aspects of arc and laser welding separately. The physics of laser welding has already been examined in Chaps. 4 and 5. A generic description of welding arcs is therefore provided here, which forms a basis for interpretation of laser-arc interactions and the hybrid welding conditions discussed in the final section of this chapter.

7.1   The Structure of the Welding Arc

Arcs belong to the class of self-sustaining reversible electrical discharges, which are characterised by plasma temperatures significantly above room temperature, high current densities at the electrodes (in comparison to other types of self-sustaining reversible electrical discharges, such as glow discharges) and relatively low voltages, of the order of a few volts to a few tens of volts. Arcs may operate over a wide range of currents from a few tens of milliampères, defining the lower boundary between arc and glow discharges, to currents of mega-ampères and above.

Arc properties and behaviour are very difficult to define precisely because of the large range of phenomena encompassed by the term. Various definitions have been proposed including the following descriptive example by Guile [1]:

I. Richardson (✉)
Department of Materials Science and Engineering, Delft University of Technology, Mekelweg 2, 2628 CD Delft, The Netherlands
e-mail: i.m.richardson@tudelft.nl

An arc is a discharge of electricity between electrodes in a gas or in a vapour from the electrodes which has a voltage drop at the cathode of the order of the excitation potential of the electrode vapour (viz: only of the order of 10 volts) and in which the current flowing can have any value almost without limit, above a minimum, which is about 100 milliampères.

Welding arcs are generally subject to additional limitations including the need for spatial and temporal stability. The subject of arc welding has been studied extensively for many years; nevertheless numerous works on the subject indicate that observation and experiment often fail to show simple or well defined behaviour, but instead provide a multitude of sometimes seemingly contradictory interdependencies, which vary enormously with prevailing conditions [1]. The physical mechanisms governing arc welding operations are numerous and involved, both within the arc and at the electrodes. Some of the observed behavioural variations can be directly ascribed to changes in conditions within the structure of the arc. Behaviour at the electrodes is known to have a major influence on arc characteristics and stability, although the exact nature of many of the interactions has yet to be fully explored.

From a macroscopic point of view the arc may be regarded as an energy converter. Energy is supplied in a controlled manner in the form of electrical input and is converted into heat and a broad range of electromagnetic radiation. The nature of the conversion process and the subsequent behaviour of the arc are determined to a large extent by the prevailing physical conditions (gas type, electrode composition, geometry etc.). In order to gain some perspective on arc behaviour it is useful to consider the main gaseous discharge characteristics required for welding operations.

The following discussion will focus on the types of arc commonly employed in welding, that is, collision dominated, stable point-plane arcs burning between a rod-like welding electrode and a planar work-piece electrode. The notation employed to describe arc and hybrid laser-arc welding is provided in Table 7.1.

7.1.1 Macroscopic Considerations

Like all gas discharges, the welding arc can be described with reference to three principal regions, the cathode fall zone, the plasma column and the anode fall zone (Fig. 7.1). These regions are not distinct but merge in a physically continuous manner. The dimensions of each of the electrode zones are of the order of 10^{-6} m. In contrast the plasma column can be several millimetres long.

The anode and cathode fall zones are characterised by net local space charges within a few microns of the electrode surfaces. The discharge contracts, giving rise to high current densities, of the order 10^8–10^9 A m^{-2} at the cathode surface and 10^7 A m^{-2} at the anode surface, whilst in the plasma column the mean current density is of the order 10^6 A m^{-2}. Differences in current density coupled with the self-induced magnetic field generate electromagnetic forces, acting from regions of high to low current density. These pump gas through the body of the discharge

Table 7.1 Table of notation

Symbol	Units	Meaning
Latin symbols		
a	m	Constant
a_o	m	Bohr radius (= 5.3×10^{-11})
A	A m^{-2} K^{-2}	Thermionic emission material constant
A_{ul}	s^{-1}	Transition probability
A_ω	V m^{-1}	Laser beam electric field amplitude
b	m	Constant
B	T	Magnetic flux density
c	m s^{-1}	Speed of light
$c_{f,r}$	m	Constant
c_p	J kg^{-1} K^{-1}	Specific heat capacity at constant pressure
C	–	Inertial coefficient
C_1	m^{-3}	Constant (7.66)
C_2	W	Material constant (7.12)
C_μ	–	Eddy viscosity proportionality constant (= 0.09)
d	m	Material thickness
d_a	m	Dendrite arm spacing
d_j	m^{-1}	Concentration gradients diffusion
D_{amb}	m^2 s^{-1}	Ambipolar diffusion coefficient
D_e	m^2 s^{-1}	Electron diffusion coefficient
D_{ij}	m^2 s^{-1}	Ordinary diffusion coefficient
$\overline{D_{AB}^x}$	m^2 s^{-1}	Combined ordinary diffusion coefficient
$\overline{D_{AB}^P}$	m^2 s^{-1}	Combined pressure diffusion coefficient
$\overline{D_{AB}^T}$	m^2 s^{-1}	Combined temperature diffusion coefficient
D_i^T	m^2 s^{-1}	Thermal diffusion coefficient
$D(E_s, W)$	–	Electron tunnelling probability
e	C	Charge on the electron
E	V m^{-1}	Electric field strength
E^a	V m^{-1}	Induced electric field
E_c	V m^{-1}	Complex electric field strength amplitude
E^e	V m^{-1}	Applied electric field
E_1	J	First ionisation energy
E_H	J	Ionisation energy of hydrogen (= 13.6 eV)
E_{iu}	J	Energy of the upper excited state
E_n	J	Discrete energy level of an atom
E_o	V m^{-1}	Electric field strength amplitude
E_s	V m^{-1}	Electric field strength at a surface
$f_{f,r}$	–	Fractional power to front and rear of Goldak ellipsoids
f_l	–	Liquid fraction
f_s	–	Solid fraction

Table 7.1 (continued)

Symbol	Units	Meaning
Latin symbols		
F_j	N	Force
F_p	m	Focal length
$\overline{g_A}$	$\text{m}^{-2}\,\text{s}^{-1}$	Mean number flux of gas A
g_i	$\text{m}^{-2}\,\text{s}^{-1}$	Number flux of ith species
g_{iu}	–	Statistical weight of the upper excited state (7.9)
g_l	–	Liquid volume fraction
g_n	–	Degeneracy of states of energy E_n
g_z	$\text{m}\,\text{s}^{-2}$	Acceleration due to gravity
$\bar{g}(\nu, T)$	–	Average Gaunt factor
$g(\nu, \text{u}_1, \text{u}_2)$	–	Gaunt factor
h	J s	Planck's constant
h, h_l	$\text{J}\,\text{kg}^{-1}$	Enthalpy
H_L	$\text{J}\,\text{m}^{-3}$	Latent heat of fusion
I	A	Current
$I(x)$	$\text{W}\,\text{m}^{-2}\,\text{sr}^{-1}$	Radiance
I_o	$\text{W}\,\text{m}^{-2}\,\text{sr}^{-1}$	Radiative power density, laser power density
$I_\nu(r, \Omega)$	$\text{J}\,\text{m}^{-2}$	Specific intensity at a position r, frequency ν in the direction Ω
$I_\lambda^o(r)$	$\text{W}\,\text{m}^{-3}\,\text{sr}^{-1}$	Plank function
$I_\nu^o(r)$	$\text{J}\,\text{m}^{-2}\,\text{sr}^{-1}$	Plank function
J	$\text{A}\,\text{m}^{-2}$	Current density
J_T	$\text{A}\,\text{m}^{-2}$	Thermionic current density
k	$\text{m}^2\,\text{s}^{-2}$	Turbulent energy
k, k_n	m^{-1}	Wave vector
k_B	$\text{J}\,\text{K}^{-1}$	Boltzmann's constant
m	–	Complex refractive index
$\overline{m_{A,B}}$	kg	Mass of gas A (or B)
m_e	kg	Mass of an electron
$M_{i,j}$	kg	Mass of an ion
$\dot{m}_v$	$\text{kg}\,\text{s}^{-1}$	Mass flux of vapour
M	$\text{kg}\,\text{mol}^{-1}$	Molar mass
n	m^{-3}	Number density
n	–	Principal quantum number (7.20)
n_a	m^{-3}	Number density of unionised atoms
n_{cr}	m^{-3}	Critical number density
n_e	m^{-3}	Electron number density
$n_{e,\,LTE}$	m^{-3}	Equilibrium electron number density
n_i	m^{-3}	Number density of species i
n_{Im}	–	Imaginary part of the refractive index

(continued)

Table 7.1 (continued)

Symbol	Units	Meaning
Latin symbols		
$\dot{n}_i$	$m^{-2}\ s^{-1}$	Number flux of particle species
n_p	m^{-3}	Aerosol particle number density
n_{Re}	–	Real part of the refractive index
n_T	m^{-3}	Number density of atoms + ions
$N(W, T_s, \varphi)$	$J^{-1}\ m^{-2}\ s^{-1}$	Supply function
P	$N\ m^{-2}$	Pressure
p_1	–	Constant (7.66)
$p(x')$	$kg\ m\ s^{-1}$	Electron momentum
P_a	$N\ m^{-2}$	Arc pressure
$P_{i,arc,laser}$	W	Power
P_p	$N\ m^{-2}$	Vapour recoil pressure
P_o	$N\ m^{-2}$	Ambient pressure
Pr	–	Prandtl number
Pr_t	–	Turbulence Prandtl number
P_s	W	Input power
P_v	$N\ m^{-2}$	Saturation vapour pressure
q	$C\ m^{-3}$	Charge per unit volume
$q_{f,\ r}$	$W\ m^{-3}$	Goldak power density distribution
q_r^{rad}	$W\ m^{-2}$	Radiative flux
Q	$W\ m^{-2}$	Power density
Q_{arc}	$W\ m^{-2}$	Arc power distribution
Q_{laser}	$W\ m^{-2}$	Laser power distribution
Q_T	$W\ m^{-2}$	Sum of laser and arc power densities
r	m	Radius
r_a	m	Arc radius
r_b	m	Laser beam radius
r_{max}	m	Maximum aerosol particle radius
r_{min}	m	Minimum aerosol particle radius
R_{ij}, R_{ji}	s^{-1}	Rate coefficients
s_i	–	Stoichiometric coefficients
S	$W\ m^{-2}$	Time averaged laser beam energy density
S_f	m^2	Laser focal spot area
S_t	s^{-1}	Strain rate
t	s	Time
T	K	Temperature
T_e	K	Electron temperature
T_s	K	Surface temperature
u	$m\ s^{-1}$	Velocity
u_E	$m\ s^{-1}$	Velocity due to electric field

(continued)

Table 7.1 (continued)

| Symbol	Units	Meaning
Latin symbols		
u_m	m s^{-1}	Metal surface velocity
u_r	m s^{-1}	Radial velocity
u_s	m s^{-1}	Surface velocity
u_t	m s^{-1}	As the characteristic turbulent velocity
u_T	m s^{-1}	Thermal velocity
u_v	m s^{-1}	Metal vapour velocity
u_w	m s^{-1}	Welding speed
u_z	m s^{-1}	Axial velocity
U	W m^{-3}	Radiation source strength
V	V	Voltage
V$_r$	m s^{-1}	Relative velocity vector between liquid and solid phases
V$_w$, V$_{sheath}$	V	Sheath voltage
W	J	Electron energy
W_a	J	Energy of an electron inside a metal
x	m	Distance to arc axis (7.8)
x_j	–	Number density ratio of jth species
y_{ref}	m	Characteristic boundary layer length
Z_i	–	Partition function
Z_j, Z_i	–	Charge number
Z	–	Ionic charge
z$_i$		Degree of ionisation, net effective charge
Greek symbols		
α	–	Fine-structure constant (= 1/137) (7.18)
α	m^2 s^{-1}	Thermal diffusivity
α$_o$	m	Bohr radius
β	m^3 K^{-1}	Volumetric expansion coefficient
γ	N m^{-1}	Surface tension coefficient
γ_g	–	Euler-Mascheroni constant
γ_k	–	Quantum yield
γ_i	–	Quantum yield
$\delta(z)$	m^{-1}	Dirac delta function
Δh	J kg^{-1}	Heat content per unit mass
ε	m^2 s^{-3}	Turbulent energy dissipation
$\varepsilon(r)$	W m^{-3} sr^{-1}	Radial emission coefficient
ε_o	A^2 s^4 kg^{-1} m^{-3}	Permittivity of free space (= 8.854×10^{-12})
ε_r	–	Dielectric constant
ε_{ul}	W m^{-3} sr^{-1}	Emission coefficient on electron transition between states u and l

Table 7.1 (continued)

Symbol	Units	Meaning
Latin symbols		
ε_ω	–	Relative complex dielectric permittivity of a plasma at frequency ω
η	–	Process efficiency
κ	W m^{-1} K^{-1}	Thermal conductivity
κ_K	–	von Karman's coefficient (= 0.4)
κ_λ, κ_ω	m^{-1}	Spectral absorption coefficient
κ_ν	m^{-1}	Radiative absorption coefficient
κ_ν^{bf}	m^{-1}	Bound-free absorption coefficient
κ_ν^{ei}	m^{-1}	Electron-ion absorption coefficient
κ_ν^{eo}	m^{-1}	Electron-atom absorption coefficient
λ	m	Wavelength
λ_L	N m^{-2}	Lagrange multiplier
μ	N s m^{-2}	Dynamic viscosity
μ_B	N s m^{-2}	Coefficient of bulk viscosity
μ_F	J	Fermi energy
μ_o	kg m s^{-2} A^{-2}	Permeability of free space (= $4\pi \times 10^{-7}$)
μ_t	N s m^{-2}	Turbulent viscosity
ν	Hz	Frequency
ν_{eo}	Hz	Electron-neutral collision frequency
ν_{ul}	Hz	Photon frequency
ρ	kg m^{-2}	Density
ρ_{ma}	kg m^{-2}	Aerosol mass density
ρ_∞	kg m^{-2}	Ambient gas density
σ	Ω^{-1} m^{-1}	Electrical conductivity
σ_c	m^2	Electron-atom collision cross section
σ_i	m^2	Photo-ionisation cross section
$\sigma_{M,a}$	m^2	Mie absorption cross section
$\sigma_{M,s}$	m^2	Mie scattering cross section
$\sigma_{R,a}$	m^2	Rayleigh absorption cross section
$\sigma_{R,s}$	m^2	Rayleigh scattering cross section
σ_T	m^2	Thomson scattering cross section
φ	V	Work function
τ_a	Pa	Shear stress
χ'	m^3 s^{-1}	Recombination coefficient
ω	s^{-1}	Angular frequency
ω_p	s^{-1}	Plasma frequency
Abbreviations		
GMA	Gas metal arc	
GTA	Gas tungsten arc	
HAZ	Heat affected zone	
LTE	Local thermal equilibrium	

(continued)

Table 7.1 (continued)

Symbol	Units	Meaning
Latin symbols		
pLTE	Partial local thermal equilibrium	
TIG	Tungsten inert gas (same as GTA)	
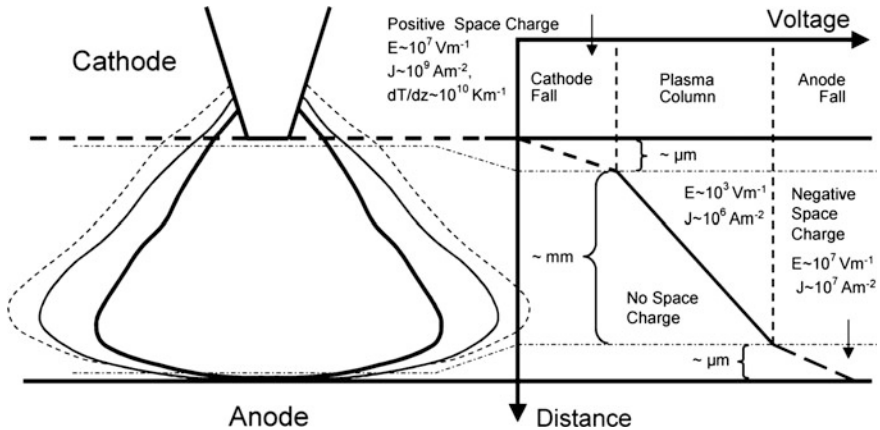
Fig. 7.1 Schematic of a point-plane welding arc structure showing order of magnitudes of dimensions, current densities, and electric field strengths in the different arc regions
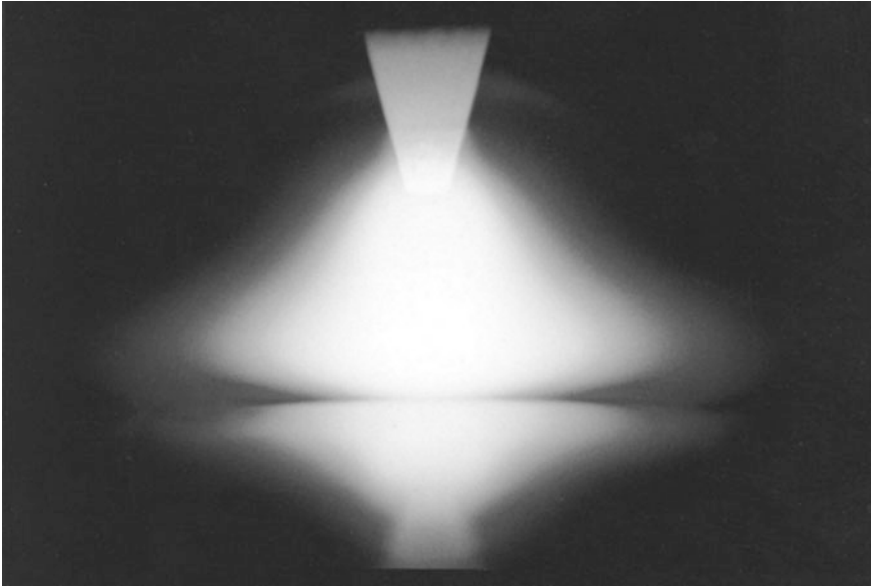
contributing to the characteristic bell shaped point-plane arc which arises (partly) as a result of colliding anode and cathode jets (Fig. 7.2).

Welding arcs are characterised by the transfer of mass between the electrodes. In consumable welding, the mass motion involves the transfer of molten metal from one electrode to another. The direction of motion is dependent on the mode of arc operation. In both consumable and non-consumable welding, gaseous products are transported through the arc. The forces generated depend on prevailing conditions near the electrodes as well as environmental conditions and boundary conditions at the edges of the discharge.

Gas flow is an important factor in welding due to its influence on process stability and resultant weld integrity. The structure and behaviour of the discharge is dependent on many factors including energy transport within the discharge, energy transfer efficiency at the electrodes, chemical reactions, species diffusion, and impurity entrainment.

To date, no comprehensive description of the physics of welding arc discharges has been constructed; the majority of approaches are based on simplifications, describing non-consumable arcs under equilibrium conditions [2]. Under such conditions the following continuity equations apply:

Fig. 7.2 Photograph of a 150 A argon gas tungsten arc burning on a stainless steel anode. The characteristic bell shape arises in part due to collision of a strong cathodic and a weak anodic plasma jet [110]

(1) Mass must be conserved

$$\frac{\partial \rho}{\partial t} + \nabla.(\rho \mathbf{u}) = 0, \tag{7.1}$$

where ρ is the mass density and $\mathbf{u}$ the velocity.

(2) Charge must be conserved

$$\frac{\partial q}{\partial t} + \nabla.\mathbf{J} = 0, \tag{7.2}$$

where q is the charge per unit volume and $\mathbf{J}$ the current density.

(3) A generalised Ohm's law applies

$$\mathbf{J} = \sigma(\mathbf{E} + \mathbf{u} \times \mathbf{B}), \tag{7.3}$$

here σ is the electrical conductivity, $\mathbf{E}$ the electrical field strength and $\mathbf{B}$ the magnetic flux density.

(4) Maxwell's equations apply

$$\nabla \times \mathbf{B} = \mu_o \mathbf{J} + \mu_o \varepsilon_o \frac{\partial \mathbf{E}}{\partial t},$$
$$\nabla \times \mathbf{E} = -\frac{\partial \mathbf{B}}{\partial t}, \qquad (7.4)$$

where μ_o is the magnetic permeability of free space and ε_o the permittivity of free space.

(5) Momentum is conserved, described by the Navier-Stokes equation for incompressible flow

$$\rho \left(\frac{\partial \mathbf{u}}{\partial t} + \mathbf{u}.\nabla \mathbf{u} \right) = -\nabla P + \mu \nabla^2 \mathbf{u} + \mathbf{J} \times \mathbf{B} + (\rho - \rho_\infty)\mathbf{g}_z, \qquad (7.5)$$

where P is the pressure, μ the dynamic viscosity, ρ_∞ the gas density outside the discharge and $\mathbf{g}_z$ the acceleration due to gravity. Here inertial terms are balanced by a pressure gradient, viscous stress, electromagnetic forces and a buoyancy force. The assumption of incompressibility requires the divergence of the flow to be zero, and is acceptable provided changes in velocity do not have a significant influence on the internal energy (temperature).
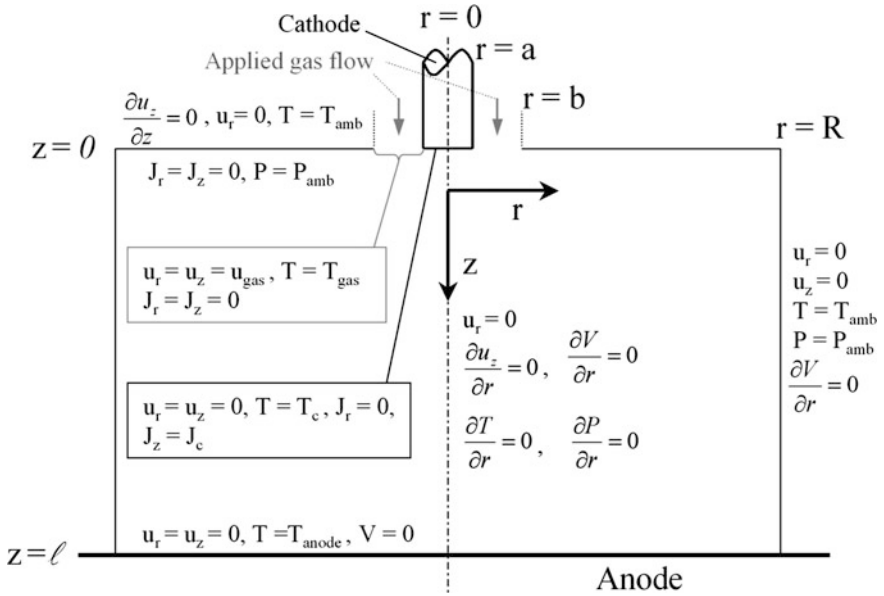
(6) Energy is conserved, thus

$$\rho \mathbf{u}.\nabla \left(h + \frac{\mathbf{u}^2}{2} \right) - \nabla.(-\kappa \nabla T) + U = \mathbf{J}.\mathbf{E}, \qquad (7.6)$$

where κ is the thermal conductivity, h the enthalpy and U the radiation source strength (energy per unit volume). Here the energy generated by the flow of electric current is balanced by enthalpy, radiative and conductive terms.

In this description density, viscosity, thermal conductivity, enthalpy and radiation source strength are thermodynamic quantities, and hence functions of temperature and pressure only for any given material.

Simultaneous numerical solutions of (7.1) to (7.6) may be used to predict the first order behaviour, structure and energy exchanges occurring in the arc column, provided the arc is reasonably stable and that some equilibrium conditions are satisfied. Boundary conditions for the solution of a stationary axisymmetric discharge are given in Fig. 7.3 (see for example [3, 4]) and typical numerical solutions for a stationary tungsten inert gas (TIG) arc operating in an argon environment are shown in Fig. 7.4. In the simplest case, the axial current density at the cathode may be assumed to be constant, although better agreement between prediction and measurement is found if the cathodic current density follows a prescribed (for example a Gaussian) distribution, or is preferably calculated directly from application of the governing equations to the body of the cathode.

The magnetohydrodynamic description outlined above does not take account of the non-equilibrium conditions occurring in the electrode fall zones, and the

Cathode $r = 0$

Applied gas flow $r = a$

$r = b$

$z = 0$

$\dfrac{\partial u_z}{\partial z} = 0 ,\ u_r = 0,\ T = T_{amb}$

$r = R$

$J_r = J_z = 0,\ P = P_{amb}$

r

z

$u_r = u_z = u_{gas},\ T = T_{gas}$
$J_r = J_z = 0$

$u_r = 0$

$u_r = 0$
$u_z = 0$
$T = T_{amb}$
$P = P_{amb}$

$\dfrac{\partial u_z}{\partial r} = 0 ,\quad \dfrac{\partial V}{\partial r} = 0$

$\dfrac{\partial V}{\partial r} = 0$

$u_r = u_z = 0,\ T = T_c,\ J_r = 0,$
$J_z = J_c$

$\dfrac{\partial T}{\partial r} = 0 ,\quad \dfrac{\partial P}{\partial r} = 0$

$u_r = u_z = 0,\ T = T_{anode},\ V = 0$

$z = \ell$

Anode

Fig. 7.3 Typical boundary conditions for numerical solution of the conservation equations governing a stationary, axi-symmetric point-plane arc. Subscript c refers to the cathode and *amb* to ambient conditions; ℓ is the distance between the cathode tip and anode plane
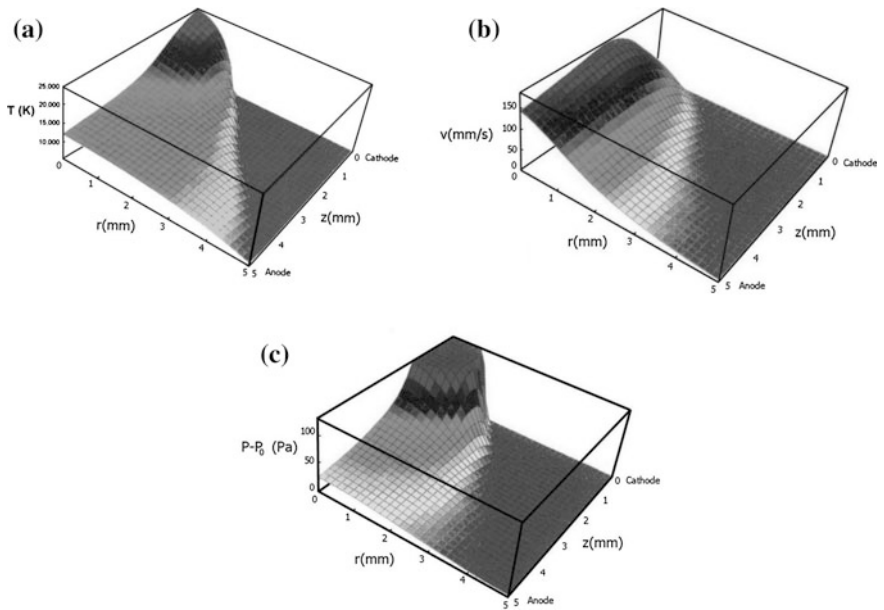
Fig. 7.4 Calculated **a** temperature **b** velocity and **c** pressure distributions for a stationary argon TIG arc. Reproduced by kind permission of the late Prof. P.D. Kapadia

description breaks down rapidly in the absence of partial local thermal equilibrium, where a multi-fluid or rate equation based approach may be better suited.

In cases where incompressibility cannot be ignored, i.e. the divergence of the flow is non-zero, the Navier-Stokes Eq. (7.5) must be modified to include extra viscous dissipation terms and takes the form

$$\rho\left(\frac{\partial \mathbf{u}}{\partial t}+\mathbf{u}.\nabla\mathbf{u}\right)=-\nabla P+\mu\nabla^2\mathbf{u}+\mathbf{J}\times\mathbf{B}+(\rho-\rho_\infty)\mathbf{g}_z+2\nabla\mu.\nabla\mathbf{u}$$
$$+\nabla\mu\times(\nabla\times\mathbf{u})+\frac{1}{3}\mu\nabla(\nabla.\mathbf{u})-\frac{2}{3}(\nabla.\mathbf{u})\nabla\mu \tag{7.7}$$
$$+\mu_B\nabla(\nabla.\mathbf{u})+(\nabla.\mathbf{u})\nabla\mu_B$$

where μ_B is the coefficient of bulk viscosity, which is assumed to be zero in the Stokes approximation [3].

7.1.2 Arc Temperatures and the PLTE Assumption

Knowledge of an arc temperature distribution provides an indication of the structure of the arc and also of the validity of the magnetohydrodynamic description. Predicted temperatures from the model of Lowke [4] are found to be in good agreement with temperatures measured by Haddad and Farmer [5] (Fig. 7.5). Maximum temperatures close to the cathode of a gas tungsten arc discharge exceed 20,000 K and temperature contours mirror the visible shape of the arc shown in Fig. 7.2. In this example, temperatures were measured by means of non-invasive emission spectroscopy, employing the Fowler-Milne method [6].

A number of spectroscopic temperature measurement techniques are available based on the relationship between the measured radiance $I(x)$ and the radial emission coefficient $\varepsilon(r)$. Assuming an optically thin, cylindrically symmetric plasma, the radial distribution of the emission coefficient can be found from the Abel inversion of measured radiance

$$\varepsilon(r)=-\pi^{-1}\int_r^R\frac{dI(x)}{dx}(x^2-r^2)^{-0.5}dx, \tag{7.8}$$

where x is the perpendicular distance between the line of observation and the axis of symmetry, r the radius and R the outer limit of the source. The intensity of a spectral line emitted upon transition of an electron from an upper to a lower energy level is proportional to the population density of the upper energy level and the transition probability. If equilibrium is assumed to hold, in other words a Boltzmann distribution is valid, then [7]

Fig. 7.5 Temperature contours of a 100 A, 5 mm long argon TIG arc. *Dashed curves* indicate experimental results [5], and *solid curves* calculations. © 2002 IoPP reproduced with permission from [4]
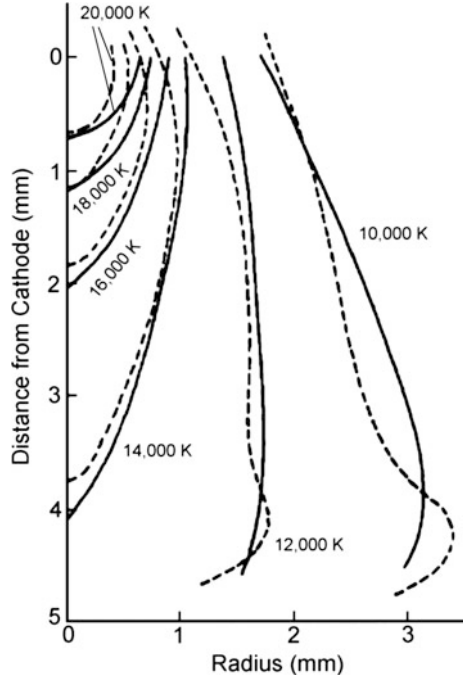
$$\varepsilon_{ul} = \frac{1}{4\pi} A_{ul} h\nu_{ul} \frac{n_i}{Z_i} g_{iu} \exp\left(-\frac{E_{iu}}{k_B T}\right), \tag{7.9}$$

where subscripts u and l refer to the upper and lower energy levels respectively. A_{ul} is the transition probability per unit time, h is Planck's constant, ν_{ul} is the frequency of the emitted photon, n_i the number density of the ith species, Z_i the partition function of the species calculated at temperature T, g_{iu} the statistical weight of the upper excited state E_{iu} the energy of the upper excited state and k_B is Boltzmann's constant.

In principle, when the emission coefficients have been measured experimentally, the temperature can be determined from (7.9); however, although frequencies, degeneracies and energy levels are often known with some precision, transition probabilities, partition functions and number densities are not always known with sufficient accuracy. To overcome difficulties with calculation of absolute line intensities, measurements may be based on relative intensities of two or more lines. In this case the ratio is independent of number densities and partition functions such that

$$\frac{\varepsilon_1}{\varepsilon_2} = \frac{A_1\nu_1 g_1}{A_2\nu_2 g_2}\exp\left(-\frac{E_1 - E_2}{k_B T}\right). \tag{7.10}$$

One problem with this approach is that the separation between the upper levels of the lines is generally of the same order or smaller than the thermal energies ($k_B T$), making the emission coefficient ratio relatively insensitive to changes in temperature. Taking neutral argon lines at 425.94 and 430.01 nm for example, an increase in temperature from 10,000 to 20,000 K alters the ratio $\varepsilon_1/\varepsilon_2$ by only 15% [8]. Improved accuracy can be obtained by measuring several line intensities and forming a Boltzmann plot [9], which yields a slope proportional to the inverse temperature, viz:

$$\ln\left(\frac{\varepsilon}{\nu Ag}\right) = -\frac{E}{k_B T} + \ln\left(\frac{hn_i}{4\pi Z_i}\right). \tag{7.11}$$

Here the second term on the right hand side is independent of the transition lines observed. Unfortunately, this method requires measurement of a large number of transition lines, significantly increasing the time required for experimental observation, and is only feasible for highly stable discharge configurations.

The expression for the radial emission coefficient (7.9) may be written in a simplified form

$$\varepsilon(T) = C_2 \frac{n(T)}{Z(T)} \exp\left(-\frac{E_{iu}}{k_B T}\right), \tag{7.12}$$

where C_2 is a constant depending only on the properties of the radiating species. The function passes through a maximum at the *normal* temperature when the increase due to the exponential term is balanced by a reduction of the particle density with temperature, resulting from both reduced density and transformation due to species ionisation. Provided the axial arc temperature exceeds the *normal* temperature, the off-axis maximum in the radial emission coefficient can be used to calibrate the radial intensity distribution. This method, known as the Fowler-Milne method [6], eliminates the need for transition probabilities and absolute equipment calibration, although the temperature dependent number density and partition function must be known. The former can be calculated from the Saha equation [7] which implicitly assumes quasi-neutrality in the plasma,

$$\frac{n_e n_i}{n_{i-1}} = 2\frac{Z_i(T)}{Z_{i-1}(T)}\left(\frac{2\pi m_e k_B T}{h^2}\right)^{3/2} \exp\left(-\frac{E_{i-1}}{k_B T}\right). \tag{7.13}$$

Here n_e is the electron density, m_e the electron mass, n_i the species density and i denotes the degree of ionisation of the species. The partition function is defined as

$$Z_i(T) = \sum_n g_n \exp\left(-\frac{E_n}{k_B T}\right), \tag{7.14}$$

where g_n is the degeneracy of states of energy E_n. The number of discrete energy levels of an isolated atom is infinite. For a plasma, the ionisation energy is reduced

due to polarisation effects of neighbouring charged particles, thus only energy levels below the reduced ionisation limit need be included. Unfortunately, there are no experimental measurements of reduced ionisation potentials, and differences in calculated particle densities arise as a result of different criteria chosen to truncate the partition function series [9].

Despite the inherent reliance of numerical models and many experimental measurement techniques on the existence of local thermal equilibrium (LTE), or at least partial local thermal equilibrium (pLTE) for which a Boltzmann distribution exists amongst the excited states of the plasma, the existence of such a condition has been questioned from both a theoretical and experimental perspective. Cram et al. [10] calculated the population density of excited states from a collisional-radiative model. Under kinetic equilibrium conditions

$$\sum_{j \neq i} \left(n_j R_{ji} - n_i R_{ij} \right) = 0, \tag{7.15}$$

where $n_i(r)$ is the population density of state i at position r. R_{ij} is the rate coefficient, comprising terms in spontaneous emission, stimulated emission and excitation and de-excitation due to particle collisions. A solution of the radiative transfer equation provides values of the net radiative (Biberman-Holstein) coefficients,

$$\frac{\partial I_\nu(r, \Omega)}{\partial l} = -\kappa_\nu(r) \left[I_\nu(r, \Omega) - I_\nu^o(r) \right], \tag{7.16}$$

where $I_\nu(r, \Omega)$ is the specific intensity at a position r, frequency ν in the direction indicated by the vector Ω. The absorption coefficient κ_ν involves continuum and line absorption terms and the source term $I_\nu^o(r)$ is given by the Planck function

$$I_\nu^o(r) = \frac{2h\nu^3}{c^2} \left[\exp\left(\frac{h\nu}{k_B T_e} \right) - 1 \right]^{-1}, \tag{7.17}$$

where c is the speed of light, and T_e the electron temperature. Differences between the population densities calculated using the LTE assumption and those of the collisional-radiative model have been found in the outer regions of the arc for electron temperatures below 8,000 K and associated electron densities below 10^{21} m^{-3}. This is attributed to enhanced excitation of higher atomic states by intense radiation emitted from the core of the arc. Strong excitation of the 4s levels occur when electron collisions are insufficient to maintain an equilibrium population due to Ar I resonance lines. Similarly, photo-recombination is responsible for exciting the ground state of the Ar II ions and the associated resonance lines enhance excitation of the excited Ar II states [10]. The electron density is below the level required for equilibrium between the ground state and excited states [9, 11]. At best, equilibrium can apply only between excited states, i.e., partial local thermal equilibrium.

Greim [7] indicates that the following condition on the electron density n_e must be satisfied for LTE to apply:

$$
\begin{aligned}
n_e &\geq \frac{5}{8\pi^{0.5}} \left(\frac{\alpha}{a_o}\right)^3 \left(\frac{E_1}{E_H}\right)^3 \left(\frac{k_B T}{E_H}\right)^{0.5} \\
&\geq 9.2 \times 10^{23} \left(\frac{E_1}{E_H}\right)^3 \left(\frac{k_B T}{E_H}\right)^{0.5},
\end{aligned}
\tag{7.18}
$$

where α is the fine-structure constant, a_o is the Bohr radius, E_H the ionisation energy of hydrogen and E_1 the plasma (first) ionisation energy. For an argon plasma with $E_1 = 2.52 \times 10^{-18}$ J and (7.18) reduces to

$$
n_e \geq 3.6 \times 10^{21} T^{0.5},
\tag{7.19}
$$

which is not attainable under welding arc conditions at atmospheric pressure.

For pLTE, the electron density condition is given by the approximation [7]

$$
n_e \geq 7 \times 10^{24} \frac{z^6}{n^{8.5}} \left(\frac{k_B T}{E_H}\right)^{0.5},
\tag{7.20}
$$

where z is the number of effective charges and n the principal quantum number. Electron densities for a given principle quantum number should meet or exceed the calculated limit to ensure that 90% of the population in that state is in equilibrium with higher discreet states and with the free electrons. Particle number densities for an argon plasma, based on the data provided in [12] are shown in Fig. 7.6.

**Fig. 7.6** Argon plasma particle number densities plotted from the data in [12]
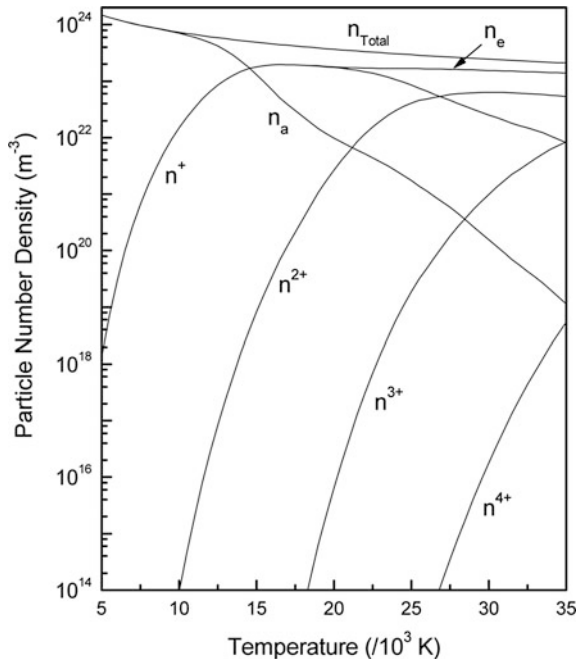
Experimental evidence for departures from pLTE has been presented by several authors [13–18]. Farmer and Haddad [13], determined argon atom number densities from experiments involving Rayleigh scattering and compared the associated temperatures with those derived by the Fowler-Milne spectroscopic technique. Significant differences, attributed to the breakdown of the Boltzmann distribution, were reported for temperatures below 9,000 K. A comparison of the maximum value of the normalised radial emission coefficient (for a 5 mm long, 200 A argon TIG arc) as a function of axial position [14], showed that although the radial emission coefficient remains constant close to the anode, departures are seen within 1.5 mm of the cathode, where the maximum value falls as the cathode is approached.

Degout and Catherinot [17] determined electron density distributions in an argon TIG arc from spectroscopic measurements of Stark broadening and compared results with absolute and two line spectroscopic methods. They concluded that pLTE did not hold anywhere within the column of a 4 mm long argon arc in the current range 25–35 A. Supporting results are reported by Thornton [9, 18] who measured the temperature of a 100 A, 5 mm long argon TIG arc using the Fowler-Milne method and found that temperatures within 1 mm of the cathode vary by up to 4,000 K dependent on the emission line employed, whilst variations of more than 1,000 K exist within the body of the discharge (Fig. 7.7). Thornton suggests that departures from pLTE within 1 mm of the cathode could be related to the reduction in electron density at temperatures exceeding 17,000 K, assuming ionisation equilibrium.

The presence or absence of pLTE in welding arc discharges has not yet been definitively established, either theoretically or experimentally. Based on the available evidence, it is certain that LTE is violated almost everywhere and it appears highly likely that significant departures from pLTE exist close to the cathode. For the remaining body of the discharge, pLTE departures, if present, are likely to be small and limited to arcs with currents of a few tens of ampères. Under these
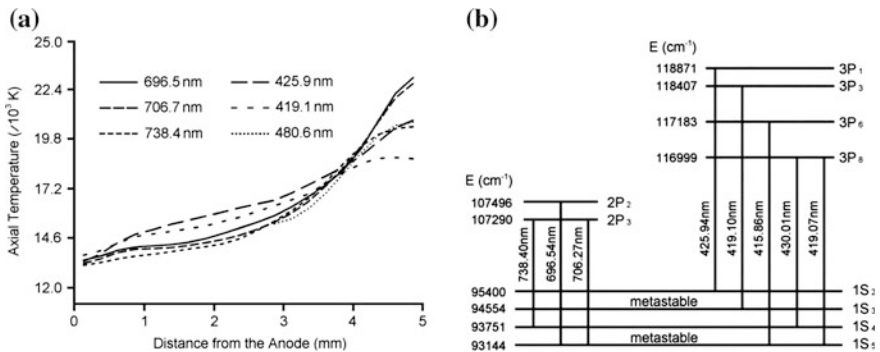
Fig. 7.7 **a** Temperatures on the axis of a 100 A, 5 mm long argon TIG arc measured for different spectral lines using the Fowler-Milne method [9] and **b** a partial energy level diagram for neutral argon

conditions it is convenient to consider such departures as errors in the derived temperature, and to model the arc based on a pLTE assumption; however, it should be noted that this may not always yield a physically relevant description of arc behaviour.

7.1.3 Multi-component Plasmas

Arc temperatures and local thermal equilibrium considerations have been discussed so far with reference to a monatomic gas. In practical welding applications, the plasma is inevitably a mixture of atomic and molecular species, the composition of which can be influenced by a number of factors including (i) the choice of shielding gas mixture; (ii) evaporation of material from the weld pool, governed primarily by weld pool chemistry, thermal distribution on the pool surface and fluid flow within the pool; and (iii) entrainment of atmospheric contaminants into the arc jet, which is a function of the shielding geometry, the momentum of the cold gas flow and velocity distribution of the arc plasma.

The local composition of a multi-species plasma is influenced by diffusive separation of component species, the plasma cannot therefore be assumed to adopt a uniform compositional distribution. For a plasma close to thermal equilibrium, the distribution function of species is assumed to be Maxwellian, perturbed by forces arising from concentration, pressure, temperature and electric field gradients associated with transport phenomena. The resultant redistribution leads to de-mixing, which in turn can influence the structure of the arc and the associated heat transfer properties.

When considering a plasma with q species, $\frac{1}{2}(q^2-q)$ linearly independent ordinary diffusion coefficients and $(q-1)$ linearly independent thermal diffusion coefficients are required to characterise the diffusion behaviour. The diffusion coefficients have to be calculated for each temperature and gas composition in the plasma, leading to $(q-1)$ species conservation and momentum conservation equations [19, 20]. In this context, a species is defined here to include electrons and any molecule, atom, or ion exhibiting a distinct structure. The large number of species present in welding plasmas means that calculations are time consuming and complex, and have yet to be reported for many welding arc compositions. Treatments can be greatly simplified if diffusion is described in terms of the gases rather than the many species present. Such an approach has been developed for a binary gas mixture by Murphy [20–23] where the $\frac{1}{2}(q^2 + q-2)$ diffusion coefficients are replaced by four combined coefficients representing (i) a combined ordinary diffusion coefficient; (ii) a combined pressure diffusion coefficient; (iii) a combined thermal diffusion coefficient, describing diffusion of the two gases due to concentration, pressure, and temperature gradients; and (iv) the electrical conductivity, describing diffusion of charged particles due to the applied electric field.

The number flux g_i of species i relative to the mass-average velocity in the presence of a temperature gradient, is given in [21] as

$$g_i \equiv n_i u_i = \frac{n^2}{\rho} \sum_{j=1}^{q} m_j D_{ij} d_j - \frac{D_i^T}{m_i} \nabla \ln T, \tag{7.21}$$

where n_i is the species number density, u_i the diffusion flux of species i relative to the mass average velocity, ρ the mass density, T the temperature and m_j the mass of the jth species. D_{ij} is the ordinary diffusion coefficient and D_i^T the thermal diffusion coefficient. The term d_j describes the diffusion forces due to gradients in concentration $x_j = n_j/n$, pressure P and external forces F_j

$$d_j = \nabla x_j + \left(x_j - \frac{\rho_j}{\rho} \right) \nabla \ln P - \frac{\rho_j}{\rho P} \left(\frac{\rho}{m_j} F_j - \sum_{l=1}^{q} n_l F_l \right). \tag{7.22}$$

Identifying the external forces with applied E^e and induced E^a electric fields to account for ambipolar diffusion yields

$$d_j = \nabla x_j + \left(x_j - \frac{\rho_j}{\rho} \right) \nabla \ln P - \frac{n_j Z_j e}{n k_B T} (E^e + E^a), \tag{7.23}$$

where $Z_j e$ is the charge on the particle. The induced electric field E^a arises due to the tendency of electrons to diffuse more rapidly than ions and acts to slow electron diffusion whilst speeding up ion diffusion.

For a mixture of gases A and B the mean number flux $\overline{g_A}$ of gas A is given by

$$\overline{g_A} = \sum_{i=2}^{q} s_i g_i = \frac{n^2}{\rho} \overline{m_B} \left(\overline{D_{AB}^x} \nabla \overline{x_B} + \overline{D_{AB}^P} \nabla \ln P \right) - \left(\frac{\overline{D_{AB}^T}}{m_A} \right) \nabla \ln T, \tag{7.24}$$

where s_i are the stoichiometric coefficients and the bar indicates that the parameters represent the gas rather than a species. The summation excludes $i = 1$ which refers to the electron contribution. Defining

$$\begin{aligned} \alpha_i &= \sum_{j=1}^{q} n_j m_j Z_j D_{ij} \\ \beta &= - \sum_{i,j=1}^{q} Z_i Z_j n_j m_j D_{ij} \end{aligned}, \tag{7.25}$$

and including the influence of the electric field in the ordinary and thermal diffusion coefficients

$$\begin{aligned} D_{ij}^a &= D_{ij} + \frac{\alpha_i}{\beta} \sum_{l=1}^{q} Z_l D_{lj} \\ D_i^{Ta} &= D_i^T + \frac{\alpha_i m_i}{\beta} \sum_{l=1}^{q} \frac{Z_l D_l^T}{m_l} \end{aligned}, \tag{7.26}$$

the combined ordinary, pressure and thermal diffusion coefficients may be expressed [21] as

$$\overline{D_{AB}^x} = \frac{1}{m_B} \sum_{i=2}^p s_i \sum_{j=1}^q m_j D_{ij}^a \frac{\partial x_j}{\partial x_B}$$

$$\overline{D_{AB}^P} = \frac{1}{m_B} \sum_{i=2}^p s_i \sum_{j=1}^q m_j D_{ij}^a \left(x_j - \frac{\rho_j}{\rho} + P \frac{\partial x_j}{\partial P} \right) . \tag{7.27}$$

$$\overline{D_{AB}^T} = \overline{m_A} \sum_{i=2}^p s_i \left(\frac{D_i^{Ta}}{m_i} - \frac{n^2}{\rho} \sum_{j=1}^q m_j D_{ij}^a T \frac{\partial x_j}{\partial T} \right)$$

Reference [24] gives the electrical conductivity as

$$\sigma = \frac{e^2 n}{\rho k_B T} \sum_{j=2}^q \left(n_j m_j Z_j D_{1j} - Z_j \sum_{i=1}^q n_i m_i Z_i D_{ji} \right). \tag{7.28}$$

The influence of diffusion-driven de-mixing in plasmas is significant under some welding conditions, for example when welding some coated materials or when welding with argon-hydrogen gas mixtures, and is also important for non-welding applications such as chemical synthesis and waste destruction. Murphy [25] reports that for a 200 A, 5 mm long TIG arc burning in an argon-helium shielding gas containing 10% helium by mass, the helium mass fraction is increased at the arc centre by 120–150%, and depleted in the outer regions of the arc by about 20%. The change in composition is accompanied by an increase in plasma flow velocity of the order 20% at atmospheric pressure [26]. This behaviour has been observed to generate high momentum plasma flows at elevated pressures, and has been exploited to extend the range of applicability of plasma keyhole welding to pressures above 90 bar [27]. For an argon-nitrogen mixture containing 20% nitrogen by mass, an increase of about 25% in nitrogen mass fraction is seen close to the axis of a 200 A TIG arc due to frictional forces driven by collisions between argon and nitrogen species. At arc radii between about 1 and 2–3 mm, a 10% mass fraction depletion is observed whilst in the outer fringes, the nitrogen mass fraction is again greater than in the input gas mixture. This is caused by diffusion driven by the mole fraction gradient, which displaces nitrogen to lower temperatures below the re-combination temperature. In general de-mixing does not have a large influence on temperatures; however, in some cases, the change in gas composition can result in significant changes in energy transport. For example for argon-hydrogen arcs, the distribution of the thermal flux to the anode can be modified causing up to 50% increased thermal flux close to the arc axis, whilst for nitrogen arcs, this increase is of the order 10% [26].

The combined diffusion coefficient approach has been extended to describe diffusion under non-equilibrium plasma conditions. The magnitudes of the combined ordinary and thermal diffusion coefficients decrease as the plasma departs from equilibrium [19, 28]; i.e., as the ratio of electron to heavy particle temperature increases. This is particularly relevant close to the cathode in arc welding.

7.2 The Arc Electrodes

The structure of an arc is determined to a significant extent by the boundary conditions at the electrodes, which in turn are governed by a large number of factors including electrode compositions, temperature distributions, chemical reactions, geometry and physical state (solid, liquid, vapour), all of which can undergo rapid and relatively large spatial and temporal variations. Local electrode conditions are governed by the composition and by the energy balance at the electrode surface, which includes terms describing particle collisions (neutral and metastable atoms and charged particles), radiation, chemical reactions, Joule heating, convection, mass transfer, conduction and vaporisation. The arc plasma changes structure close to the electrodes to ensure continuity at the interface.

7.2.1 The Cathode

The extent of the cathode fall region can be estimated from the values of the cathode voltage drop and electric field strength (Fig. 7.1), which imply a thickness of the order 10^{-6} m; this is at most of the order of the mean free paths of the component particle species, indicating a negligible collision rate and energy transfer within this region [29].

The current density at the cathode surface is the sum of the ionic and electronic terms, where the latter includes contributions from both primary and secondary emission mechanisms. For refractory cathodes, emission behaviour is often described by the Richardson-Dushman equation for thermionic emitters modified to include a Schottky contribution. Taking account of secondary terms the electronic current density J takes the form [30]

$$J = e \sum_i \gamma_i \dot{n}_i + A T^2 \exp\left(- \frac{e\varphi}{k_B T} + \frac{e}{k_B T} \left(\frac{eE}{4\pi \varepsilon_r \varepsilon_o} \right)^{0.5} \right), \qquad (7.29)$$

where γ_i is the quantum yield and $\dot{n}_i$ the number flux of particle species i arriving at the cathode surface (including photons), φ is the work function, A a material constant and ε_r the dielectric constant. The relative influences of electric field strength and temperature are shown in Fig. 7.8.

The high temperature at the cathode is maintained by the energy flux carried by particles diffusing to the cathode surface, driven by density and potential gradients; on reaching the cathode these are neutralised, absorbed or undergo de-excitation. The particle flux required for current continuity exceeds the supply from the plasma column and the combined cathode sheath and pre-sheath potential reflects the energy required to generate sufficient flux in the vicinity of the cathode due to collisions between the gas and emitted electrons.

Fig. 7.8 Current density as a function of temperature and electric field strength for an arc burning on a cathode with a 4.5 eV work function. © 2002 IoPP reproduced with permission from [31]
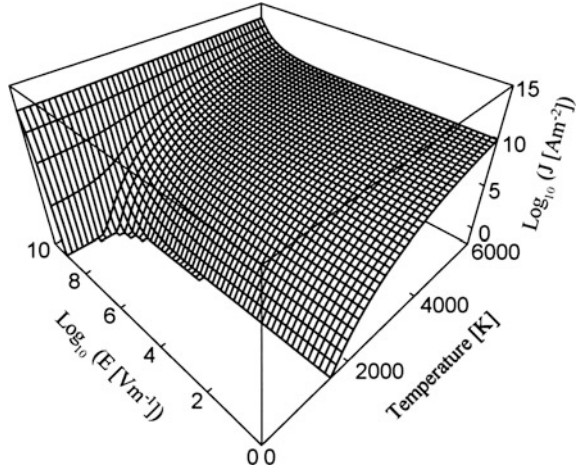
In order to provide an adequate model of the cathode sheath region, the population densities, distributions and collision cross-sections of all species present should be determined together with the energy balance equation. Several models of varying degrees of complexity have been reported [29–36] and many factors play a role. For example, the presence of ions close to the cathode surface leads to a two stage resonant tunnelling process, involving metal to ion and ion to sheath steps, which effectively lower the local potential barrier. A rate equation approach [33] has been adopted to show that the resonant contribution significantly exceeds the non-resonant term and that ion neutralisation and re-ionisation play an important role in the space charge region. This observation is in agreement with the earlier model of Hsu and Pfender [34] who indicate a sharply increasing ion flux within 10 μm of the cathode surface. The temperature is reported to rise sharply away from the surface, increasing from the melting temperature of the electrode to 10^4 K over a distance of around 5 μm [32].

For non-thermionic cathodes, similar physical considerations apply; however, it is generally accepted that the balance shifts toward the domination of field emission as the primary mechanism. The Murphy and Good equation is often employed [37, 38], which takes the form

$$J = e \int_{-W_a}^{\infty} D(E_s, W)\, N(W, T_s, \varphi)\, dW, \tag{7.30}$$

where $D(E_s, W)$ is the electron tunnelling probability and $N(W, T_s, \varphi)$ is the number of Fermi-Dirac distributed electrons incident on the barrier per unit time per unit area having energy between W and $W + dW$. The effective potential energy of the electrons inside the metal is $-W_a$; T_s is the cathode surface temperature and E_s the electric field strength at the surface. The Richardson-Schottky expression is

recovered when $E_s \rightarrow 0$. The effect of ions close to the cathode surface can be taken into account by multiplying the right hand side of the above expression by an enhancement factor dependent on temperature, ion density and ionic charge. In the above expression

$$D(Es, \ W) = \left[1 + \exp\left(-i\frac{4\pi}{h}\int_{x_1}^{x_2} p(x')dx'\right)\right]^{-1}$$

and

$$N(W, T_s, \ \phi)dW = \frac{4\pi m k_B T}{h^3}\ln\left\{1 + \exp\left(-\frac{(W-\mu_F)}{k_B T}\right)\right\}dW, \qquad (7.31)$$

where m_e is the electronic mass and μ_F the Fermi energy, x' the direction normal to the cathode surface and the integration limits x_1 and x_2 are defined at zeros in the square of the momentum function [37]. This description is valid for a simple boundary.

7.2.2 The Anode

In common with the cathode region, the arc contracts near the anode and a thin, non-equilibrium region exists close to the electrode surface. The high current density compared with the plasma column drives an electromagnetic anode jet, which opposes the (generally) stronger cathode jet, contributing to the typical bell shaped discharge (Fig. 7.2). Unlike the cathode, the current at the anode surface is carried almost entirely by electrons. Positive ions are created within the anode sheath primarily due to collisions and the sheath exhibits a concentration gradient ranging from almost zero at the anode surface to approximately equal numbers of ions and electrons adjacent to the plasma column. The energy balance in the sheath region, together with continuity considerations determine the detailed structure of the sheath.

The energy flux at the anode includes terms for radiation arriving from the plasma, radiative emission from the surface [32], collisions with neutral and metastable particles, and electron condensation; the latter being the dominant term [39]. The current density in the anode sheath includes a diffusion term, which dominates at low temperatures in the absence of equilibrium, when the electrical conductivity would otherwise be insufficient to maintain the current flow. The current density may be expressed as.

$$J = -\sigma E + eD_e\nabla n_e, \qquad (7.32)$$

where D_e is the electron diffusion coefficient. The electron continuity equation is dependent on the ambipolar diffusion coefficient D_{amb}, which accounts for electron diffusion in the local electric field, and may be written [40–42]

$$\nabla . D_{amb} \nabla n_e + \chi^{'} \left[n_{e,LTE}^2 - n_e^2 \right] = 0, \tag{7.33}$$

where $n_{e,LTE}$ is the equilibrium electron number densities and χ' is the recombination coefficient, which takes the form given by Hinnov and Hirschberg [42, 43]

$$\chi^{'} = 1.1 \times 10^{-20} n_e T_e^{-9/2} \left[\text{m}^3 \text{s}^{-1} \right]. \tag{7.34}$$

Some uncertainty exists over the numerical factor in the above expression; a value of 1.1×10^{-24}, derived from the same source is quoted in [42], whilst [44] quotes 8.72×10^{-22}, which includes corrections for additional terms.

Boundary conditions applied to solve (7.33) assume that n_e takes the equilibrium value at the plasma interface, whilst at the electrode surface

$$n_e = \frac{J_T}{e u_T}, \tag{7.35}$$

where J_T is the thermionic emission current density and u_T is the thermal velocity where $u_T = (8 k_B T / \pi m_e)^{0.5}$; see [40]. Solutions of the continuity equation [45] lead to negative electric field strengths in the anode sheath and negative effective electrical conductivities for the diffuse anode root typically observed during welding [32, 44–47]. For constricted arc roots, positive electric field strengths are predicted and both positive and negative conditions have been inferred from measurements based on Langmuir probe [46] and Thomson scattering experiments [47].

7.3 Fluid Flow in the Arc-Generated Weld Pool

Fluid flow in the weld pool may be modelled using the same basic continuity equations used to describe the body of the arc; see Sect. 7.1 and examples in [48–52]. For the majority of models, a laminar flow regime is assumed. A number of forces act on the pool; these include the Lorentz force F_{em}, which has a vertical component driving flow downward from the centre of the weld pool, proportional to $J_r B_\theta$. The buoyancy force F_B is given by

$$F_B = -\rho_m g_z \beta (T - T_m), \tag{7.36}$$

where T_m is the melting temperature of the pool ρ_m the density at the melting point and β the volume expansion coefficient. The surface tension force is usually added

as a boundary condition and is dependent on the shape of the pool surface. The associated Marangoni-driven flow [48] may be described as

$$-\mu \frac{\partial u_s}{\partial n} = \tau_a + \frac{d\gamma}{dT} \frac{\partial T}{\partial s}, \tag{7.37}$$

where u_s is the surface velocity and τ_a the shear stress acting on the base plate. The static force balance accounting for surface deformation may be written as

$$\gamma \left\{ r \frac{\partial^2 z}{\partial r^2} + \frac{\partial z}{\partial r} \left(1 + \left(\frac{\partial z}{\partial r} \right)^2 \right) \right\} = r \left(1 + \left(\frac{\partial z}{\partial r} \right)^2 \right)^{\frac{3}{2}} \{ \rho g_z z - P_a + \lambda_L \}, \tag{7.38}$$

where P_a is the arc pressure and λ_L is the Lagrange multiplier, which is modified between iterations to satisfy the required continuity constraints. The work piece is assumed to act as a uniform current sink with zero potential gradient at all boundaries except the weld pool surface; current flow due to the location of the return connection to the welding power source, which is known to be influential in practical welding applications, is therefore ignored. Kim and Na [48] predict outward toroidal fluid flows and weld pool surface oscillations due to current pulsing for TIG arcs operating on a 304 stainless steel substrate. The outward flow leads to the formation of wide and shallow weld pools. For peak pulsed currents up to 160 A and a 2 mm long argon arc, the heat flux and current distribution have the same radii and a Gaussian-like distribution, with peak values in the range 1.8– 9.3 $\times$ 10^{-6} W m^{-2} and 1.8–9.6 $\times$ 10^{-6} A m^{-2} respectively. The arc pressure peaks at the pool centre and lies in the range 50–550 Pa, whilst the shear stress due to the gas flow across the anode surface peaks at a radius of just over 1 mm and lies in the range 35–90 Pa. Fluid flow velocities, both inside the weld pool and on the surface are of the order 0.1–0.25 m s^{-1}.

Some attention has been paid to the possibility of turbulent flow in the weld pool, which has been examined by Chakraborty et al. [52] among others, who included a Reynolds stress term $\partial \left(-\rho \overline{u_i' u_j'} \right) / \partial x_j$ in the Navier-Stokes equations. Here i and j indicate directions and the prime indicates velocity fluctuations. Turbulence is modelled using the classical eddy viscosity k-ε model, where the Reynolds stress term is given by

$$\left(-\rho \overline{u_i' u_j'} \right) = \mu_t \left(\frac{\partial \overline{u}_i}{\partial x_j} + \frac{\partial \overline{u}_j}{\partial x_i} \right) - \frac{2}{3} \delta_{ij} \rho k, \tag{7.39}$$

and the turbulent viscosity μ_t is dependent on the liquid fraction f_l

$$\mu_t = C_\mu f_l^{0.5} \rho \frac{k^2}{\varepsilon}, \tag{7.40}$$

providing a smooth transition from the solid to the liquid state. Here C_μ is the eddy viscosity proportionality constant, k denotes the turbulent kinetic energy and ε the turbulent kinetic energy dissipation rate. The turbulent heat flux $\left(-\overline{u_j'T'}\right)$ appearing in the energy balance equation is

$$\left(-\overline{u_j'T'}\right) = \frac{\mu_t}{\rho \, \mathrm{Pr}_t} \frac{\partial \overline{T}}{\partial x_j}, \tag{7.41}$$

where Pr_t is the turbulent Prandtl number (taken to be 0.9). The standard governing equations for k and ε are employed and values of k and ε have been estimated based on a scaling analysis. The surface velocity of the weld pool is found to be

$$u_s \approx \left(\frac{\eta Q}{\pi r_a^2 \rho c_p} \frac{\partial \gamma}{\partial T} \frac{1}{\mu}\right)^{0.5}, \tag{7.42}$$

where Q is the arc power, η the process efficiency and r_a the arc radius. The characteristic boundary layer length is

$$y_{ref} \approx \left(\frac{\eta Q}{\pi r_a^2 \rho c_p} \frac{r_a c_p}{u_s \Delta H}\right), \tag{7.43}$$

where ΔH is the heat content per unit mass. In a quasi-steady state the rate of turbulent energy production is approximately the same as the dissipation rate hence

$$C_\mu \frac{k^2}{\varepsilon} S_t^2 = C_\mu \frac{k^2}{\varepsilon} \left(\frac{u_s}{y_{ref}}\right)^2 \approx \varepsilon, \tag{7.44}$$

where S_t is the strain rate. Defining u_t as the characteristic turbulent velocity fluctuation

$$u_t = \kappa_K C_\mu^{0.5} u_s, \tag{7.45}$$

where ρ_K is von Kármán's coefficient, k and ε are respectively

$$k \approx u_t^2 = \kappa_K^2 C_\mu u_s^2;$$
$$\varepsilon \approx \frac{u_t^3}{\kappa_K y_{ref}} = C_\mu^{0.5} k \frac{u_s}{y_{ref}}. \tag{7.46}$$

The position of the maximum dissipation of turbulent energy within the weld pool is dependent on the prevailing surface tension gradient. In the case of an inward toroidal flow (positive $\partial \gamma / \partial T$), k and ε are reported to reach maxima near the melt front due to the high local thermal gradients and velocities driven by the Marangoni flow. Conversely for an outward toroidal flow (negative $\partial \gamma / \partial T$),

the turbulent kinetic energy and dissipation terms are highest close to the weld pool edges transverse to the welding direction, again where the temperature gradients are high. As the turbulent kinetic energy generation is proportional to the square of the strain rate, the maximum velocities occur in the regions of highest temperature gradients and are therefore coincident with the regions of maximum energy dissipation.

In the case of positive $\partial\gamma/\partial T$ (inward toroidal flow) the weld pool penetration reaches a maximum further away from the pool centre than is observed in a laminar flow regime, and penetration is reduced due to the reduced momentum of the fluid carrying heat from the surface of the pool in the downward direction. The molten zone of the turbulent weld pool is also shorter than in the laminar case, which may be attributed to increased thermal diffusion. For a negative surface tension gradient, the maximum penetration is greater for turbulent flow than for laminar flow, due to increased thermal diffusion and reduced momentum [52, 53].

7.4 Unified Arc and Electrode Models

Modelling of the welding arc is motivated by a number of goals, amongst which are a desire to understand the physics of the arc and to explain the behaviour of the discharge under different operating conditions. Another rationale is to predict the performance of welding processes based on physical principles. This remains a daunting task because of the complexity of processes involved and their widely differing length and time scales. With the continuing improvement in numerical efficiency and computational speed, models unifying discharge and electrode conditions have become feasible in the past decade and some aspects of welding process behaviour are now amenable to numerical prediction.

Some simplifications are inevitable when modelling a complex system. For example, Zhu et al. [45] present an analysis of free burning arcs including the electrodes with an emphasis on anode properties. The non-equilibrium sheath region at the anode is treated by approximation in which the iteration grid size is chosen large enough to include the electron diffusion region (estimated to be of the order 40 μm), the electrical conductivity is assumed to be equal to that of the adjacent plasma and the energy balance equation is solved for zero electric field strength. Simplification of the cathode sheath structure has also been described [42] where the energy balance equation in the sheath is neglected, as are space charge considerations and the ionisation term due to electron acceleration in the electric field. In this work only the electron continuity equation involving ambipolar diffusion was considered together with thermal ionisation and recombination. Electron emission is assumed to be thermionic and radiative heating of the electrodes was neglected. Current densities are derived for the combined arc and electrode region from the current continuity equation, without prior assumption of the current density distribution at the cathode surface. The relative influence of several factors on the surface temperature of the cathode are shown in Fig. 7.9 [42]. It can be seen

Fig. 7.9 Predicted
temperatures on the cathode
surface for a 200 A argon *TIG
arc* indicating the role of
various heat-transfer
processes. Experimental
points (*circles*) are taken from
[60]. © 2002 IoPP reproduced
with permission from [42]
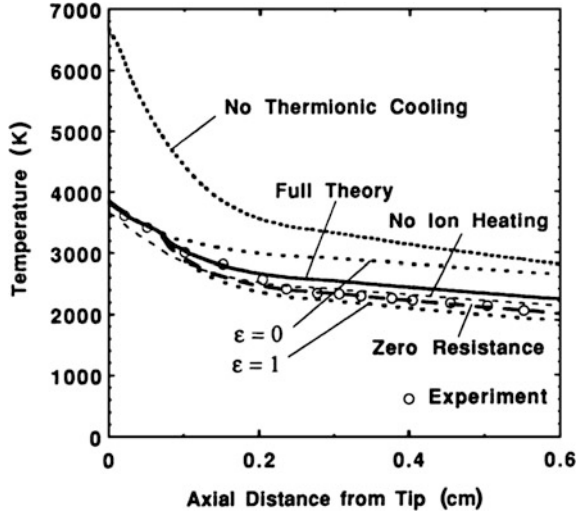
that results are fairly insensitive to the heating effects of the ions and to Ohmic
heating (zero resistance). Emissivity has a notable influence and has been calculated
for the extremes of 0 and 1, whilst the largest influence is seen from the transpi-
ration (thermionic) cooling term, which is critical for the prevention of melting at
the electrode surface.

The influence of welding parameters on weld pool formation has been examined in
a number of studies [40, 54–62]. Goodarzi et al. [54, 55] employed a simplified
treatment of the cathode and anode sheaths and showed a maximum anode heat flux at
an electrode angle of about 60° for a 200 A, 2 mm long argon TIG arc; whilst for 5
and 10 mm arc lengths, the heat flux shows a much weaker tip angle dependency.
Shear stress on the anode surface due to convective gas flow is predicted to decrease
from 250 to 200 Pa as electrode tip angle increases from 10° to 60° for a 2 mm arc
length. The same trend is observed for longer arcs, although the peak shear stress,
which occurs at an arc radius of around 1.25 mm, is reduced to 210 to 175 Pa for a
5 mm long arc. The results contrast somewhat with those of Tanaka et al. [57] where a
peak shear stress of 38 Pa is predicted for a 5 mm long, 150 A argon TIG arc.
A number of factors may contribute to this discrepancy, including differences in
sheath treatments at the electrodes and neglecting buoyancy in the arc plasma in [54].

Ushio et al. [40] predict weld pool fluid flow with positive and negative surface
tension gradients, corresponding to inward and outward toroidal flows (high and
low sulphur conditions) on a 304 stainless steel. Resulting fusion zone shapes are in
qualitative agreement with experimental observations. In a later paper, the authors
examine possible mechanisms responsible for increases in weld penetration due to
the addition of a surface flux [58]. The following four mechanisms are proposed:
(i) a change in surface tension which reverses the temperature dependent surface
tension gradient to generate an inward flow; (ii) electron depletion in the outer
fringes of the arc due to liberated flux ions, resulting in an increase in current

density; (iii) reduced surface tension resulting in greater pool depression and (iv) insulation of the weld pool surface away from the arc axis due to the presence of an oxide layer. Mechanisms (i) and (iv) are shown to be possible contributory factors. Electron depletion due to the ion flux (ii) was accounted for by adding terms for oxygen—electron collisions and oxygen ion—metal atom electron liberation to the electron continuity equation. The resulting calculations however showed that this is not a significant mechanism. The limitation of the model to a flat anode surface assumption meant that it was not possible to assess the pool depression and arc pressure influence, although experimental observations suggest that such an influence is small at welding currents below 150 A. This also suggests that increases in arc velocity due to core acceleration driven by de–mixing processes is likely to be small, although this aspect was not explicitly included in the model.

Multi-component plasmas have been included in the unified models of Lago et al. [61, 62] and Tanaka et al. [63]. In the former work, the mass flux $\dot{m}_v$ from the vaporising anode surface is represented by

$$\dot{m}_v = \frac{1}{1 - X_i} \rho D_v \frac{\partial X_i}{\partial z}, \qquad (7.47)$$

evaluated at the anode surface. Here D_v is the diffusion coefficient of the metal vapour in the plasma and the X_i is the vapour mass fraction given by

$$X_i = \frac{P_v M_m}{P_v M_m + (1 - P_v) M_p}, \qquad (7.48)$$

where P_v is the saturation vapour pressure and M the molar masses of the metal and plasma (subscripts m and p respectively). Metal vapour ingress into the arc is shown to be limited to the region adjacent to the anode surface due to the dominance of the cathode jet [61, 63]. The presence of the vapour leads to a reduction in plasma temperature, which may be explained in terms of the lower ionisation potential compared with the plasma.

Unified arc and electrode models offer the potential to explore the influence of physical phenomena and boundary conditions on arcs and weld pools. To date, most of the unified models reported assume a stationary anode surface, which is likely to underestimate the influence of arc shear on weld pool flow. Free surfaces have however been considered for the description of metal droplet transport in Gas Metal Arc (GMA) welding [64–67] to describe the evolution of the metal droplet as well as droplet absorption at the molten weld pool surface. In these models the influence of the droplet on the plasma is considered but the plasma is treated as an LTE fluid and vaporisation and diffusion of metallic components within the plasma, which may be expected to have a significant influence, are generally ignored.

7.5   Arc Plasma-Laser Interactions

The combination of a laser with an arc discharge for welding purposes was first described by Steen and co-workers in the late 1970s [68, 69]. Since that time, considerable attention has been paid to the experimental characteristics and possible applications of hybrid laser-arc processes. A number of different process combinations have been examined including lasers with the gas tungsten arc, gas metal arc and plasma arc welding processes, with a range of geometries and laser wavelengths. In the following discussion, attention will be focus primarily gas (CO_2) and solid-state (Nd:YAG) laser interactions with the welding arc.

When a laser beam and a plasma interact, a number of effects are possible. From the perspective of the laser beam, the beam may be absorbed in the arc plasma, scattered or defocused, generally resulting in a decrease in laser power impinging on the work piece in comparison to laser operation in the absence of the arc. From the perspective of the arc, energy can be absorbed from the laser beam in the plasma column, resulting in a change in electrical structure, flow field and temperature. Laser energy may also be absorbed at the arc root, changing the structure of the sheath, the energy transport to the work piece surface, and modifying the temperature, fluid flow behaviour and metallic vapour distribution in the upstream plasma. In the case of a cathodic work piece, laser radiation can also modify the electron emission mechanisms, increasing thermionic emission due to a local increase in surface temperature and will modify the ionic contribution to thermo-field emission due to changes in the particle energy distribution in the cathode sheath.

The balance of radiative energy gain and loss by the plasma may be expressed by replacing the radiative source strength in the energy balance (7.6) by a term describing the divergence of the radiative flux q_r^{rad}. Deron et al. [70] define this term for a one-dimensional axisymmetric plasma as

$$\frac{1}{r}\frac{d}{dr}\left(rq_f^{rad}\right) = \int_{\lambda^{-1}} d\lambda^{-1}\kappa_\lambda(r)\left\{4\pi I_\lambda^o(r) - \int_{r'}\kappa_\lambda(r')I_\lambda^o(r')\exp\left(-\Theta\right)\frac{dr'}{\|r'-r\|^2}\right\},$$

(7.49)

where

$$\Theta = \int_{s=0}^{\|r'-r\|}\kappa_\lambda\left(r+s\frac{r'-r}{\|r'-r\|}\right)ds.$$

Here $\kappa_\lambda(r)$ is the spectral absorption coefficient of the plasma at position r, and wavelength λ, $I_\lambda^o(r)$ the Planck function at temperature $T(r)$ and s the optical path.

7.5.1 Absorption

Laser light is absorbed in a plasma as a result of inverse bremsstrahlung due to bound-free and free-free transitions. For typical welding arc plasmas with a Maxwellian electron velocity distribution and relatively low electron temperatures (no more than a few eV), the linear absorption coefficient for light of frequency ν due to electron ion collisions is given by [71, 72]

$$\kappa_\nu^{ei} = \bar{g}(\nu, T) \left(\frac{2\,\pi\,m_e}{3\,k_B T_e} \right)^{0.5} \left(\frac{Z^2}{n_{Re}} \right) \frac{n_e n_i e^6}{6\,c\,h(2\pi\varepsilon_o \nu)^3 m_e^2} \left[1 - \exp\left(-\frac{h\nu}{k_B T} \right) \right], \quad (7.50)$$

where n_{Re} is the real part of the complex refractive index of the plasma Z the ion charge and $\bar{g}(\nu, T)$ the averaged Gaunt factor. This expression is only valid provided the radiation field does not perturb the electron velocity distribution from a Maxwellian state. The influence of the radiation can be assessed by examining the ratio of electron velocities due to thermal and electric field contributions. The acceleration experienced by an electron in the radiant electric field is $eE_o sin(\omega t)$ and the corresponding maximum speed u_E is $|eE_o/m_e\omega|$. The electric field is related to the intensity I_o (power per unit area) by $I_o = \frac{1}{2}\,\varepsilon_o c E_o^2$ and the thermal velocity u_T is of the order $(3k_B T_e/m_e)^{0.5}$, the ratio of electrical to thermal velocities is therefore

$$\frac{u_E}{u_T} = \frac{\lambda}{T_e^{0.5}} \frac{e}{\pi c} \left(\frac{I_o}{6m_e\varepsilon_o c\,k_B} \right)^{0.5} \quad \ll \quad 1 \quad (7.51)$$

for CO_2 and Nd:YAG laser radiation at any temperature with reasonable electron density and for laser power densities to 10^{12} W m^{-2} or higher. The averaged Gaunt factor in (7.50) is often expressed as

$$\bar{g}(\nu, T) = \frac{\sqrt{3}}{\pi} \ln \left[\left(\frac{2}{\gamma_g} \right)^{\frac{5}{2}} \left(\frac{k_B T_e}{m_e} \right)^{\frac{3}{2}} \left(\frac{2\varepsilon_o m_e}{Ze^2 \nu} \right) \right], \quad (7.52)$$

where γ_g is the Euler-Mascheroni constant (=1.781), and is valid provided $h\nu \ll k_B T_e$, which is just about acceptable at temperatures above 10^4 K for CO_2 laser radiation at 10.64 μm, but is not valid for Nd:YAG laser radiation at the low electron temperatures (≤ 2 eV) typically encountered in arcs. For the shorter wavelength Nd:YAG radiation of 1.06 μm, the Born approximation is also invalid at such low temperatures and a quantum mechanical description is required.

For a non-relativistic electron making a transition from speed u_1 to speed u_2 [71], the Gaunt factor due to Sommerfeld is

$$g(\nu, u_1, u_2) = \frac{\sqrt{3}\,\pi\,x\frac{d}{dx}|F(i\eta_1, i\eta_2, 1; x)|}{\{\exp(2\pi\eta_1) - 1\}\{1 - \exp(-2\pi\eta_2)\}},\qquad(7.53)$$

where

$$\eta_{1,2} = \frac{Ze^2}{2\varepsilon_o h\nu_{1,2}};\quad x = -\frac{4\eta_1\eta_2}{(\eta_2 - \eta_1)^2}$$

and

$$F(\alpha, \beta, \gamma; x) = 1 + \frac{\alpha\beta}{\gamma}\frac{x}{1!} + \frac{\alpha(\alpha+1)\beta(\beta+1)}{\gamma(\gamma+1)}\frac{x^2}{2!} + \cdots.$$

A functionally equivalent form, avoiding the differential term in the above expression was employed by Paulini and Simon [72] for numerical simplicity

$$g(\nu, u_1, u_2) = \frac{\sqrt{3}\,\pi\,\eta_2\eta_1}{\{\exp(2\pi\eta_1) - 1\}\{1 - \exp(-2\pi\eta_2)\}}\frac{\Psi(i\eta_1, i\eta_2)}{(\eta_2 - \eta_1)},\qquad(7.54)$$

with

$$\Psi(i\eta_1, i\eta_2) = F^2((1 - i\eta_1), -i\eta_2, 1:x) - F^2((1 - i\eta_2), -i\eta_1, 1; x)$$

For a Maxwellian distribution of electron velocities, the average Gaunt factor is

$$\bar{g}(\nu, u_1, u_2) = \exp\left(\frac{h\nu}{k_B T_e}\right)\int_{\frac{h\nu}{k_B T_e}}^{\infty} g(\nu, u_1, u_2)\,\exp(-\tau)d\tau,\qquad(7.55)$$

where

$$\tau = \frac{E}{k_B T};\quad E = \frac{1}{2}mu_1^2;\quad E - h\nu = \frac{1}{2}mu_2^2.$$

Many approximations can be found in the literature, ranging from the purely numerical expressions to simplifications of the Sommerfeld quantum mechanical description; see (7.53). For example, Seyffarth and Krivtsun [73] present a frequency independent factor proportional to $\ln(Tn^{-1/3})$, Wang and Rhodes [74] quote a factor proportional to $\ln(T^{4/3}P_e^{-1/3})$ where P_e is the electron pressure, whereas Greim [7] indicates a $\ln(T^3\lambda^2)$ dependency where $\omega \ll \omega_p$, which is invalid for CO_2 and Nd:YAG lasers irradiating welding arcs for which the plasma frequency ω_p is of the order 10^{12}–10^{13} s^{-1}. A numerical approximation for the

Table 7.2 Coefficients $a_{n,m}$ for calculation of the Gaunt factor: see (7.56) [75]

m	0	1	2
n	0.1 μm $\leq \lambda \leq$ 1 μm		
0	1.1740	0.0662	0.0217
1	0.1982	0.4819	0.2240
2	0.3230	0.0454	−0.0831
	1 μm $\leq \lambda \leq$ 100 μm		
1	1.1750	0.0789	0.1842
2	0.1812	0.5586	0.0304
3	0.3305	0.0203	0.0657

Gaunt factor is presented by Stallcop and Billman [75], for electron temperatures ≥ 1 eV which takes the form

$$g(\lambda, T) = \sum_{n,m} a_{n,m} (\log_{10} T/Z^2)^n (\log_{10} Z^2 \lambda)^m, \qquad (7.56)$$

where Z is the ionic charge and coefficients $a_{n,m}$ are given in Table 7.2. and typical values are shown in Fig. 7.10.

A number of expressions for the absorption coefficient may be found in the literature, which differ from (7.50) in greater or lesser detail; see for example [73–75]. Deron et al. [70] for example present the same expression without accounting for refractive index or the net charge the (Z^2/μ) term. These authors also describe absorption coefficients for electron-atom κ_ν^{eo} and bound-free κ_ν^{bf} contributions of the form:
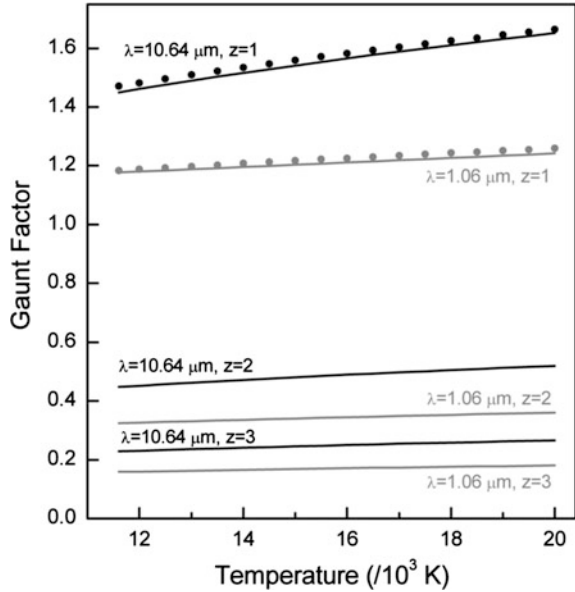
$$k_\nu^{eo} = \frac{4e^2 n_e n_o}{3 \pi \varepsilon_o hc\nu^3} \left(\frac{k_B T}{2\pi m_e}\right)^{\frac{3}{2}} \sigma_c(T) \left[1 - \exp\left(-\frac{h\nu}{k_B T}\right)\right] \left[1 + \left(1 + \frac{h\nu}{k_B T}\right)^2\right], \quad (7.57)$$

$$\kappa_\nu^{bf} = \left[1 - \exp\left(\frac{h\nu}{k_B T}\right)\right] \sum_i n_i \sigma_i(\nu),$$

where $\sigma_c(T)$ is the electron-atom collision cross section [76] and $\sigma_i(\nu)$ photo-ionisation cross-section. For CO_2 and Nd:YAG laser irradiation of a gas plasma, κ_ν^{bf} is small. Temperature dependent absorption coefficients for an argon plasma are shown in Fig. 7.11.

The complex refractive index of an isotropic plasma can be expressed as the difference of the real and imaginary components by Appleton's equation [77, 78]

Fig. 7.10 Gaunt factors for
different wavelengths and
charges for an argon plasma.
Points are plotted from the
numerical approximation in
[72] and lines from (7.56)
[75]

$$\Phi = \left(\frac{\omega_p^2}{\omega^2 + \nu_{eo}^2} \right)$$

$$n_{Re} = \left\{ \frac{1}{2} (1 - \Phi) + \frac{1}{2} \left[(1 - \Phi)^2 + \frac{\nu_{eo}^2}{\omega^2} (\Phi)^2 \right]^{0.5} \right\}^{0.5} ,$$ (7.58)

$$n_{Im} = \left\{ -\frac{1}{2} (1 - \Phi) + \frac{1}{2} \left[(1 - \Phi)^2 + \frac{\nu_{eo}^2}{\omega^2} (\Phi)^2 \right]^{0.5} \right\}^{0.5}$$

where ν_{eo} is the electron-neutral collision frequency, ω the angular frequency of the incident radiation and ω_p the plasma frequency. The collision frequency can be estimated from

$$\nu_{eo} = n_o \sigma_c \left(\frac{3k_B T_e}{m_e} \right)^{0.5}; \quad \omega_p = \left(\frac{n_e e^2}{\varepsilon_o m_e} \right)^{0.5},$$ (7.59)

where σ_c is the electron-atom collision cross section [76]. The critical damping factor γ_c of a plasma is related to the number density of atoms and ions n_T and can be estimated from

$$\gamma_c \approx \sigma_c n_T \left(\frac{3k_B T}{m_e} \right)^{0.5}.$$ (7.60)

For an argon plasma, angular plasma frequencies range from 6.9×10^{12} s^{-1} at 10,000 K to a maximum of 2.5×10^{13} at around 16,500 K falling to 2.4×10^{13} s^{-1} at 20,000 K. The angular frequency of the laser radiation is

Fig. 7.11 Calculated absorption coefficients based on (7.50) and (7.57) using number densities from [12] and collision cross sections from [76]
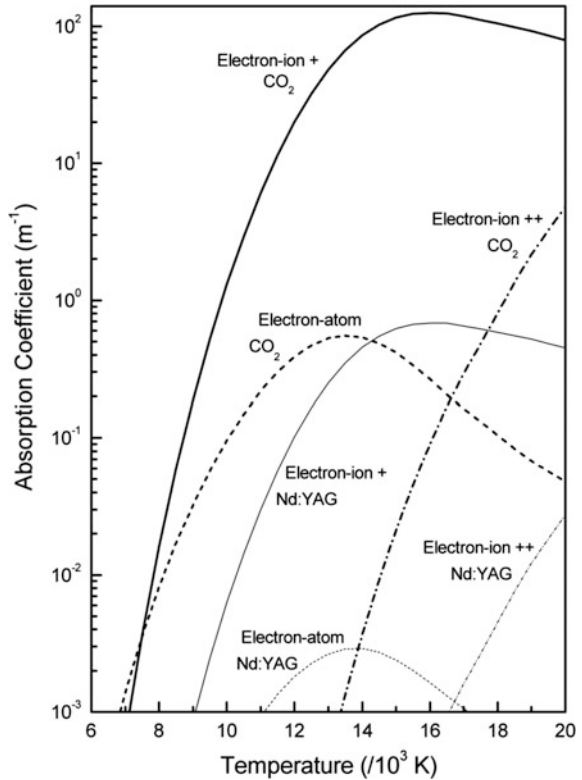
2.8×10^{14} s^{-1} and 2.8×10^{13} s^{-1} for Nd:YAG and CO$_2$ lasers respectively. In both cases $\omega > \omega_p$, $\gamma_c \ll \omega_p$ and the plasma is dispersive. For the CO$_2$ laser, as ω approaches ω_p, and the plasma approaches resonance.

The real part of the refractive index remains very close to unity, whilst the absorption coefficient κ_ν [79] approximated by

$$\kappa_\nu = \frac{4\pi n_{\mathrm{Im}}}{\lambda},\tag{7.61}$$

is small for Nd:YAG laser radiation and the laser undergoes minimal defocusing in the plasma. For the longer wavelength CO$_2$ radiation, the real part of the refractive index also remains close to unity, whilst the absorption coefficient becomes non-negligible, as plasma temperature increases.

7.5.2 Scattering

The principal scattering mechanisms relevant to laser-arc plasma interactions are Rayleigh scattering, involving particles much smaller than the wavelength of the incident radiation, and Mie scattering from particles of a similar size or larger than the incident wavelength. Thomson scattering from electrons is independent of wavelength and has a cross-section σ_T [71], which is negligibly small.

$$\sigma_T = \frac{8\pi}{3}\left(\frac{e^2}{4\pi\varepsilon_o m_e c^2}\right) = 6.65 \times 10^{-29}[\text{m}^2], \qquad (7.62)$$

Rayleigh scattering occurs from particles that act as dipoles in the electric field. For uniform spherical particles of radius r, both scattering and absorption can take place, which is dependent on the complex refractive index m of the plasma, but not on the internal refractive index of the scattering particles. The respective scattering and absorption cross sections are [80]

$$\sigma_{R,s} = \frac{3}{2\pi}\left(\frac{2\pi}{\lambda}\right)^4\left(\frac{4\pi r^3}{3}\right)^2\left|\frac{m^2-1}{m^2+2}\right|^2$$

$$\sigma_{R,a} = \frac{6\pi}{\lambda}\left(\frac{4\pi r^3}{3}\right)\text{Im}\left(\frac{m^2-1}{m^2+2}\right). \qquad (7.63)$$

Greses and co-workers [81, 82] indicate that for a laser wavelength of 1.03 μm and iron vapour with a complex refractive index m of $3.81 + 4.44i$ and particle radius of 20 nm, the scattering cross-section is 6.9×10^{-19} m^2, the absorption cross-section is 5.7×10^{-17} m^2 and measured beam attenuations of 4–40% are reported for a range of Nd:YAG laser welding conditions. The linear attenuation coefficient is the product of the cross-section and the particle density, which for an iron vapour plume in laser welding is of the order 10^{18} m^{-3} [82]. Similar orders of magnitude may be expected for laser-TIG and laser-plasma hybrid welding where the laser heat source has a significantly higher surface power density than the arc source. In the case of consumable arc welding, the particle size distribution [83] is much broader than that measured during laser welding [82], with peak number densities occurring for particles in the range 0.1–0.5 μm [83, 84].

Mie scattering, from particles of diameter similar to or greater than the incident wavelength, can also be treated as scattering from discrete dipoles. However, such large particles are represented by dipole arrays instead of single dipoles. For particles irradiated by non-polarised light, the scattering and absorption cross-sections [85] are

$$
\sigma_{M,s} = \frac{8\pi r^6}{3} \left(\frac{2\pi}{\lambda}\right)^4 \left|\frac{m^2-1}{m^2+2}\right|^2
$$
$$
\sigma_{M,a} = \frac{8\pi^2 r^3}{\lambda} \mathrm{Im}\left[\left(\frac{m^2-1}{m^2+2}\right)\left(1+\frac{2\pi r}{\lambda}\left(\frac{m^2-1}{m^2+2}\right)\frac{m^4+27m^2+38}{2m^2+3}\right)\right]. \tag{7.64}
$$

The corresponding linear attenuation coefficients can be found by multiplying the cross-sections by the particle density or, for non-uniform particle sizes, a particle distribution function $n_p(r)$ (in units of m^{-3}), which describes the number of particles per unit volume and per unit radius as a function of the radius r. Thomas [85] provides a simple size distribution function for aerosols with a range of particle radii

$$
n_p(r) = A r^\alpha \exp(-b r^\gamma), \tag{7.65}
$$

where A, b, α, and γ are constants and the particle number density is $n_p = A\gamma^{-1} b^{-(\alpha+1)/\gamma} \Gamma((\alpha+1)/\gamma)$. Mie scattering in laser welding has been studied by Hansen and Duley [86], with particular reference to the vapour in the keyhole during welding. These authors describe the particle density with an expression of the form $n_p(r) = C_1 r^{p_1}$ where C_1 and p_1 are constants, and examined the relative roles of scattering and absorption due to Nd:YAG and CO_2 laser irradiation. The mass density of aerosol material ρ_{ma} is described by

$$
\rho_{ma} = \begin{cases} \frac{4\pi C_1 \rho}{3(p_1+4)}\left(r_{max}^{p_1+4} - r_{min}^{p_1+4}\right) & p_1 \neq -4 \\ \frac{4\pi C_1 \rho}{3}\ln\left[\frac{r_{max}}{r_{min}}\right] & p_1 = -4 \end{cases}, \tag{7.66}
$$

where ρ is the internal density of the aerosol particles and subscripts *max* and *min* refer to the maximum and minimum particle sizes. The linear absorption and scattering coefficients are proportional to the ratio ρ_{ma}/ρ and attenuation for Nd: YAG laser radiation becomes significant when ρ_{ma}/ρ approaches 10^{-4}, corresponding to particle number densities of 1.9×10^{14} and 1.9×10^{11} m^{-3} for particle sizes of 0.5 and 5 μm respectively. These compare with particle densities of the order 10^{12}–10^{11} m^{-3} reported for GMA welding [82], indicating that Mie Scattering can potentially modify the power density distribution during laser-GMA welding. Absorption by the aerosol particles results in heating which is estimated to be of the order 10^7 K s^{-1} ($\rho_{ma}/\rho = 10^{-4}$, $\lambda = 10.6$ μm, $I_o = 10^{10}$ W m^{-2}), particles therefore vaporise in less than 1 ms. The contribution of Mie scattering will therefore be determined to a large extent by the rate of particle production. Mie scattering in CO_2 laser welding has been observed experimentally by Tu et al. [87] using a 363.8 nm wavelength probe laser close to the edge of the plume, where transmittance fell to below 20%, compared with over 60% in the plume centre.
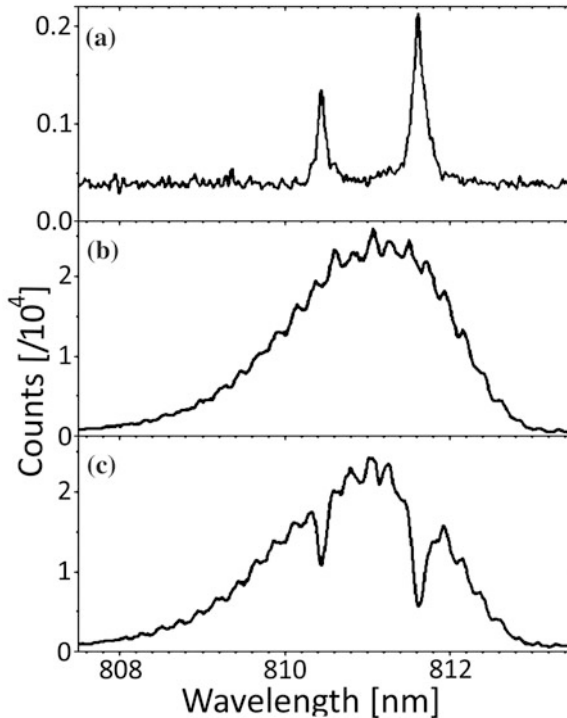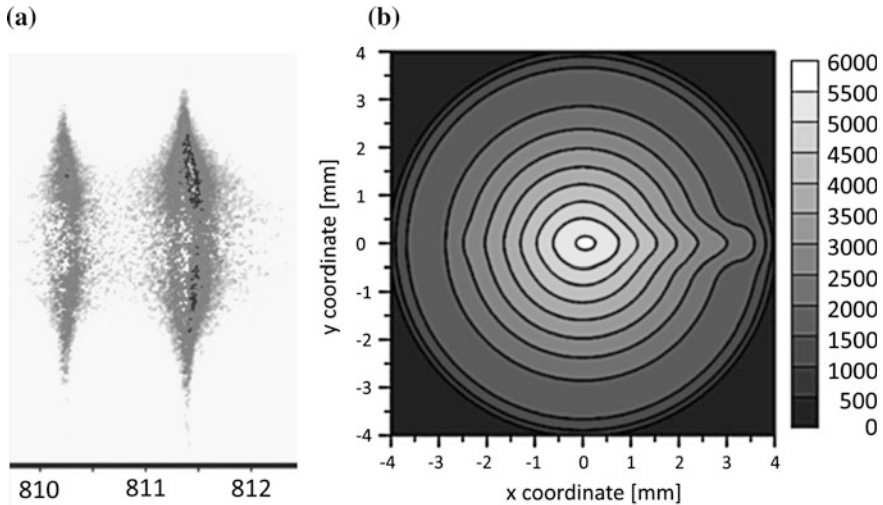
Fig. 7.12 Measured spectra of **a** a 120 A argon TIG arc, **b** a 367 W Nd:YAG laser and **c** the combined laser and arc. Reproduced from [88] with permission of IOP Publishing in the format Book via Copyright Clearance Center

7.5.3 Absorption Measurements

Kozakov et al. [88] examined the influence of a Nd:YAG laser beam oriented transverse to the axis of a non-consumable TIG arc. Spectral measurements for the arc in the absence of the laser beam are shown in Fig. 7.12a, illustrating two argon atomic lines at 810.4 and 811.5 nm. The line widths (full width half maximum) are less than 0.2 nm are much smaller than the width of the laser in the absence of the arc, Fig. 7.12b, which has a full width half maximum of 2.5 nm.

When the laser passes through the arc, corresponding absorption peaks are observed; see Fig. 7.12c. Comparison of the curves shows that scattering and refraction is negligible in comparison to absorption, as might be expected in the absence of fumes or metal vapour. The power absorption was reported to be of the order 16% of the incident beam power, viz. ~59 W, corresponding to about 5% of the total arc power, with spectral measurements indicating that absorption takes place preferentially in the cooler outer regions of the arc (Fig. 7.13a, [88]), where population density of the initial state of the resonant transitions is highest. The associated change in electrical conductivity is shown in Fig. 7.13b, [89].

Fig. 7.13 a Difference between spectra measured with and without 367 W Nd:YAG laser irradiation on an 8 mm long, 120 A argon TIG arc. The vertical axis represents the cross-sectional plane, 4 mm above the anode surface [88]. **b** Electrical conductivity profile [$\Omega^{-1}\,m^{-1}$] for the same arc and laser configuration. Reproduced from [89] with permission of Springer

Spectral methods have also been employed in the study of beam absorption in the plasma during laser welding with a CO_2 laser (see Chap. 5), indicating that absorption is dependent on the shielding gas flow rate, which in turn influences the distribution of metal vapour in the plume [90]. Absorption was reported to decrease from over 40% at a flow rate of 1 litre per minute to 15% at a flow rate of 8 litres per minutes for the experimental configuration considered. Results imply that the energy distribution during laser-arc hybrid welding is strongly dependent upon the characteristics of the processes involved and the prevailing boundary conditions.

7.6 Laser-Arc Hybrid Welding

Various terminologiesare used to classify laser-arc interactions including laser enhanced arc welding and arc augmented laser welding. The first of these indicates that the majority of the power is derived from the arc discharge, whilst the opposite is true for the latter. In the intermediate regime, the generic term laser-hybrid welding is generally employed, which also encompasses the arc and laser dominated regimes.

Steen and co-workers [68, 69] first showed that in comparison to laser welding alone, arc augmented laser welding can deliver increased welding speeds of 50–100% when combining a CO_2 laser with a TIG arc. They also showed increased penetration and observed that the arc root on a planar anode showed affinity for the

laser focal spot. Compared with non-augmented laser welding, a further benefit of greater tolerance to joint geometry variations for combined process operation has been found. The commercial development of laser-arc welding began only after the widespread industrial acceptance of laser welding in the early 1990s, and to some extent rested on the development of laser optics and arc welding torches suitable for combined process applications. In recent years, a great deal of research effort has been expended on assessment of these processes to characterise their performance and explore potential advantages. Practical aspects of laser-arc applications are addressed in many published works, which are reviewed for example in [91]. The limited literature available addressing hybrid process modelling focuses either on laser-plasma interactions or discusses the influence of combined heat sources.

In an uncoupled model of heat transfer in laser-TIG welding Chen et al. [92, 93] describe the laser and arc as independent heat sources, with a reduction of the arc radius to account for the influence of the laser on the arc. The laser energy is distributed inside the keyhole according to

$$Q_{laser} = I_o \exp\left(-2\frac{r^2}{r_b^2}\right) \exp(-\kappa_\nu z),$$
$$r^2 = (x - u_w t)^2 + y^2$$

(7.67)

where u_w is the welding speed, I_o the peak power density at the beam centre and r_b the beam radius. The beam power P_{laser} is therefore

$$P_{laser} = \int_0^{2r_b} \int_0^Z Q_{laser} 2\pi r \, dr \, dz.$$

(7.68)

In this model, energy from the arc is assumed to be distributed over the weld pool surface according to

$$Q_{arc} = \frac{3\eta VI}{\pi r_a^2} \exp\left(-3\frac{r^2}{r_a^2}\right),$$

(7.69)

where V is the voltage, I the current, η the process efficiency and r_a the arc radius. The thermal distribution in the work piece was derived for prescribed heat fluxes at the upper and lower surfaces. Predictions from this simple model indicate that at the surface, the heating rate and maximum surface temperature for a 1 kW laser beam ($r_b = 1$ mm) is dominated by the laser conditions, whilst the arc has comparatively little influence. Inside the keyhole, the heating rate due to hybrid operation rises faster with increasing depth than that found for laser welding without arc augmentation, resulting in deeper penetration. Penetration increases initially with arc current, but decreases again at high current, which is ascribed to arc broadening due to laser power absorption.

Numerical simulation of heat flow in conduction mode laser-GTA welding has also been reported by Hu [94], where the arc heat source is represented by a
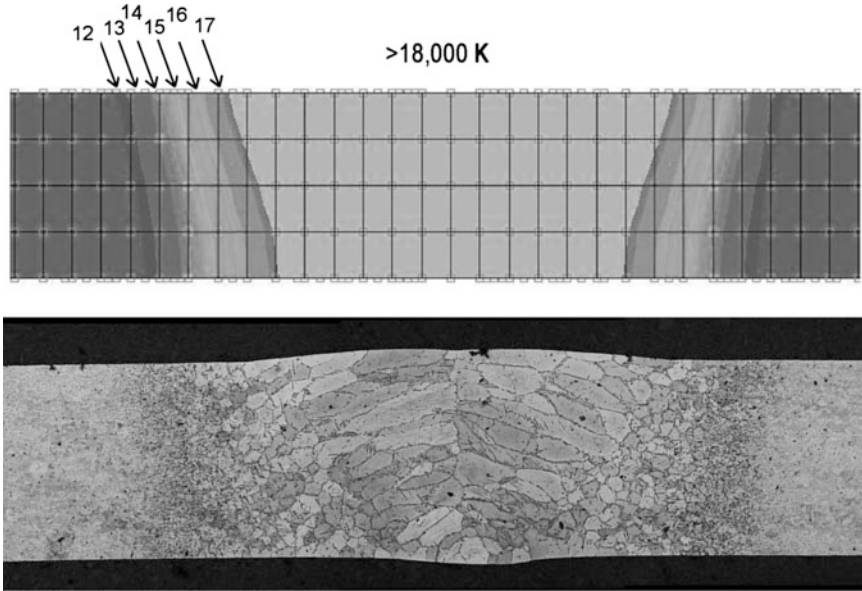
Fig. 7.14 Predicted thermal distribution and associated microstructure for a laser-TIG weld made on a 1 mm thick low carbon steel (FeP04) at 20 mm s^{-1} travel speed [94]. Numbers indicate temperatures (/10^3 K)

Gaussian surface flux term, and the laser heat source by a Gaussian volume flux term. The thermal gradient in the heat affected zone of a hybrid weld was simulated using measured values of laser beam and arc root radii and energy transfer coefficients as model inputs. Although fluid flow was not explicitly incorporated in the calculation, the temperature profiles of the weld metal and heat-affected zone agree well with measured thermal distributions and reflect the structure observed in associated weld metal cross sections. A comparison of time spent at temperatures giving rise to significant grain growth showed a reduction of 40% when comparing arc and hybrid welds on a 1 mm thick low carbon steel, resulting in reduced HAZ grain size, consistent with experimental observation. An example of the model temperature profile and corresponding weld microstructure is shown in Fig. 7.14.

A similar study has been reported for a Nd:YAG laser and GMA arc hybrid process by Reutzel et al. [95] in which the thermal distributions for the arc, the laser and the hybrid condition are described by Goldak double ellipsoid volumetric terms [96] viz:

$$q_{f,r}(x,y,z,t) = \frac{6\sqrt{3}f_{f,r}P_s}{abc_{f,r}\pi^{1.5}}\exp\left(-3\frac{x^2}{a^2} - 3\frac{y^2}{b^2} - 3\frac{(z+u_w t)^2}{c_{f,r}^2}\right), \tag{7.70}$$

where u_w is the welding velocity in the z direction, P_s the input power, a, b and $c_{f,r}$ are constants, subscripts f and r refer to the front and rear ellipsoids and $f_{f,r}$ to the

fraction of the total heat input assigned to each ellipsoid such that $f_f + f_r = 2$. Good agreement was reported for the arc case; however the model predicted weld pool widths 35% greater than those obtained from experiments for full penetration laser welds in a 5 mm thick steel substrate. Direct combinations of laser and arc parameters were found to be inappropriate to describe the hybrid case, which required adjustment of the distribution parameters. These observations are in agreement with the expectation that the combined presence of a laser and arc result in a modified power distribution, which in turn has an influence on convective heat transport (fluid flow) in the weld pool.

The hydrodynamic processes in a weld pool have been considered semi-analytically by Zaĭkin et al. [97]. Radial fluid velocities on the surface of the weld pool were measured by direct observation, whilst axial velocities were inferred by scaling the radial values by the pool depth divided by the pool radius. The average vapour recoil pressure $\langle P_p \rangle$ is estimated from

$$\langle P_p \rangle = P_o + \frac{u_m u_v}{S_f}, \tag{7.71}$$

where u_m is the velocity of the metal, u_v the velocity of vapour expansion and S_f the focal spot area. Changes in mean vapour recoil pressure due to a measured fluid flow velocity of 0.75 m s^{-1} are in the order 1 kPa. Variation in mass transport within the weld pool results in periodic changes of the vapour recoil pressure due to oscillation of the volume of the keyhole. For a CO_2 laser power density of 2×10^{10} W m^{-2}, experimentally measured oscillation frequencies in the range 10^2–10^3 Hz were found, which satisfy the condition $g\rho/\gamma k_n \ll 1$, where ρ is the density, γ the surface tension and k_n the wave number, and hence may be described as capillary waves. It is possible that such waves form due to the periodic absorption and defocusing of the laser by the plasma jet, the properties of which then oscillate due to the periodic change in metallic vapour concentration expelled from the keyhole.

The influence of synergistic interactions between a laser and an arc has also been studied semi-analytically by Paulini and Simon [72] who examined the energy balance at the anode for a laser-TIG process. Their model assumes a Gaussian current density distribution at the work piece surface, with an arc radius of 2 mm. The laser power distribution is also assumed to be Gaussian, with a radius of 0.1 mm, and absorption takes place due to inverse bremsstrahlung and Fresnel processes (see Sect. 7.1) for perpendicularly incident light. Latent heat and fluid flow are neglected and it is assumed that the weld pool surface is substantially unaffected by the laser beam; i.e., that no keyhole forms. The problem then reduces to finding a solution for the stationary heat conduction equation with a summed laser and arc power distribution $Q_T(x, y)$

$$u_w \frac{\partial T}{\partial x} = \alpha \nabla^2 T + \frac{Q_T(x, y)}{\rho\, C_p} \delta(z), \tag{7.72}$$

where α is the thermal diffusivity, u_w the welding speed and $\delta(z)$ the Dirac delta function. For a work piece of finite thickness d, and a boundary condition of zero thermal gradient at the lower surface of the plate $(z = -d)$, an analytical solution can be found of the form [98, 99]

$$T = T_o + \sum_{i=laser,\,arc} \left(\frac{P_i}{\kappa\, r_i\, \pi^{1.5}} \sum_{n=-\infty}^{\infty} \int_o^\infty \frac{d\tau}{1+\tau^2} \exp\{\Xi(\tau,n)\} \right),$$

$$\Xi(\tau,n) = \left\{ \frac{-\tau^2}{1+\tau^2} \left[\left(\frac{x}{r_i} - \frac{r_i u_w}{4\alpha\tau^2} \right)^2 + \left(\frac{y}{r_i} \right)^2 \right] - \tau^2 \left(\frac{z}{r_i} - 2n\frac{d}{r_i} \right)^2 \right\}$$

(7.73)

where κ is the thermal conductivity and the heat sources are moving in the positive x direction. The minimum arc power required to make a full penetration weld occurs when the melting isotherm intersects the lower surface of the work piece at a single point. For typical welding speeds of a few millimetres per second and in the absence of a laser, arc powers in the range 200–500 W are required to penetrate a 1 mm thick steel sheet, and surface temperatures lie in the range 1900–2100 K, well below the vaporisation temperature, which is of the order 3000 K. Some constraint is required to specify arc and laser powers uniquely for laser enhancement of the TIG arc, and this is chosen as the condition under which the weld pool surface $(z = 0)$ reaches the vaporisation temperature. Upon vaporisation, metal ions are released into the arc, altering the arc structure and modifying the energy density at the work piece surface. For a minimal full penetration condition, the laser power required to achieve surface vaporisation is substantially independent of welding speed and for a steel work piece is 65 W for a Nd:YAG laser and 130 W for a CO_2 laser. For aluminium alloys, the minimum laser powers increase by a factor of 6 whilst for copper, the minimum requirement is over 2 kW at 10.6 μm and over 3 kW at 1.06 μm [72]. The threshold laser powers are strongly dependent on the chosen arc and laser radii and on the temperature averaged material properties employed, and neglect laser absorption and scattering from the arc plasma. However, they indicate that for welds made on steel, changes in arc structure and energy transport may be expected at relatively modest beam powers.

Experimental measurements indicating changes in arc structure due to laser enhancement have been reported by Hu and den Ouden [100] who show direct photographic evidence of arc contraction due to metal vapour liberation and report calorimetric measurements of heat transfer to the work piece in laser, arc and hybrid welds. The heat dissipation measurements show no difference in heat transfer between the sum of the laser and arc sources acting separately and a hybrid process operation. However, the melting efficiency, defined as the percentage ratio of power required to heat and melt the weld volume obtained per unit time to the total power transferred to the work piece per unit time, is found to be 30–50% above the melting efficiency for the equivalent laser and arc conditions where the processes operate separately. These observations are consistent with the role of metal vapour in the arc plasma and have been confirmed by Langmuir and surface probe measurements

made in TIG arcs with and without laser addition, which show a decrease in the conductive radius and increase in current density in the laser-arc condition.

The interaction between a laser beam and the arc plasma column has been examined by Dowden and Kapadia [101] by means of an analytical energy balance approach, where consideration is given to extreme conditions. Ohmic heating dominates at the plasma temperatures occurring in an arc without laser irradiation, producing sufficient heating for ionisation and current flow. At low laser powers the laser acts to stabilise the plasma and helps to define the arc path, but provides only a small fraction of the energy required for ionisation. In contrast, at high plasma temperatures and laser powers, inverse bremsstrahlung provides a significant contribution to the energy required for current continuity. Under such conditions, inverse bremsstrahlung can dominate, opening a high conductivity path for current flow. However, laser powers, of the order several tens to hundreds of kilowatts are necessary to achieve such a condition and these lie above the limits usually available for welding applications.

Plasma interactions at laser powers of up to 1.5 kW have been examined by Startsev et al. [102] for a co-axial and axi-symmetric hybrid plasma configuration, involving a cylindrical hollow cathode. The interaction was modelled by inclusion of an absorption coefficient in the energy balance equation, which—cf (7.6)—took the form

$$
\begin{aligned}
&\frac{\partial}{\partial z}\left(\rho c_p T\, r\, u_z\right) - \frac{\partial}{\partial r}\left(-\rho c_p T\, r\, u_r\right) - \frac{\partial}{\partial z}\left(\frac{\mu}{\mathrm{Pr}} r \frac{\partial}{\partial z}\left(c_p T\right)\right), \\
&- \frac{\partial}{\partial r}\left(\frac{\mu}{\mathrm{Pr}} r \frac{\partial}{\partial r}\left(c_p T\right)\right) + r\left(\sigma E^2 + \kappa_\nu Q_{laser} - U\right) = 0
\end{aligned}
\tag{7.74}
$$

where Pr is the Prandtl number and Q_{laser} the incident laser power density. The propagation of the laser is treated as a quasi-planar electromagnetic wave propagating in the z direction, thus

$$
\frac{\partial^2 E_c}{\partial z^2} + 2ik\frac{\partial E_c}{\partial z} + \frac{1}{r}\frac{\partial}{\partial r}\left(r\frac{\partial E_c}{\partial r}\right) + k^2\left(-\frac{n_e}{n_{cr}} + i\frac{\kappa_\nu}{k}\right)E_c = 0,
\tag{7.75}
$$

where E_c is the complex amplitude of the electric field, k the wave vector, n_e the electron number density, n_{cr} the critical electron number density. The first term in right most parentheses, involving electron density ratio describes refraction, whilst the second term describes absorption. The plasma is assumed to be in pLTE and the electron density is therefore derived from the Saha equation. The electric field amplitude is related to the laser power density Q_{laser} by

$$
Q_{laser} = \frac{1}{2}\left(\frac{\varepsilon_o}{\mu_o}\right)^{0.5} E_c^2,
\tag{7.76}
$$

and the argon plasma radiation is related to the temperature by

$$U = \frac{280P^2 z^2}{(T \times 10^{-4})^{2.5}} \left(1 + 2.7 \times 10^{-6} T\right), \tag{7.77}$$

where P is the pressure and z the degree of ionisation. The laser beam profile is assumed to be Gaussian with a focal spot radius of r_f at a focal plane $z = F_P$ (in the absence of a plasma) and the spatial distribution of the complex amplitude of the electric field is defined as

$$E_c = \left(\frac{4P_{laser}}{\pi r_f^2}\left(\frac{\mu_o}{\varepsilon_o}\right)^{0.5}\right)^{0.5} \frac{r_f}{r_z} \exp\left(-\frac{r^2}{r_z^2} + i\left(\frac{kr^2}{2R_z} - \phi_z\right)\right), \tag{7.78}$$

where

$$
\begin{array}{ll}
r_z^2 = r_f^2\left(1 + \left(\frac{z - F_p}{z_f}\right)^2\right); & R_z = (z - F_P)\left(1 + \left(\frac{z_f}{z - F_p}\right)^2\right) \\
\phi_z = \tan^{-1}\left(\frac{z - F_p}{z_f}\right); & z_f = \frac{1}{2}k r_f^2.
\end{array}
\tag{7.79}
$$

This system of governing equations has been solved numerically for suitable boundary conditions using an iterative technique whereby a solution for the arc is sought, followed by a solution for the laser propagation; see (7.76). The process is repeated until all the required convergence criteria are satisfied.

The results indicate a significant temperature rise in the core of the arc. For a cathode with a 4 mm internal diameter and 6 mm external diameter, an arc length of 5 mm and an argon plasma, the core arc temperatures are 10,000–12,000 K for currents of 50–200 A, in the absence of the laser. With the 1.5 kW CO_2 laser, the core temperature rises to 18,000–21,000 K, which is accompanied by enhanced ionisation and hence greater electrical conductivity. As a result, the current density at the anode increases from 7×10^6 A m^{-2} to 4.5×10^7 A m^{-2} for a 100 A arc and the voltage drop in the arc column decreases by 25–50%. Whilst the current path changes, the gas flow is only weakly affected, with axial and radial velocities changing by less than 5%. The absorption coefficient and refractive index of the plasma are dependent on temperature and show significant spatial variation within the arc column. Increasing current results in increased absorption, but also in increased refraction due to the temperature dependence of the dielectric permeability, which governs the refractive index; see for example (7.58) and (7.59). For a 200 A arcing condition, this results in self-focusing of the beam on the arc axis and enhanced beam intensity in comparison to laser conditions in the absence of the arc.

A drop in arc voltage due to the impingement of a co-axial laser beam has been observed experimentally by Mahrle et al. [103] for a 40 A plasma arc irradiated by a 200 W fibre laser. Voltage drops of between 5 and 10% were noted dependent on substrate material and operating conditions. The voltage differences reported for co-axial irradiation differ from those reported for transverse irradiation, where changes of the order a few millivolts [88] to a few tens of millivolts [89]

are reported, the differences being attributable to the absence of electrode influences in the latter case.

Reisgen et al. [104] have examined the change in TIG arc plasma properties under conditions most often employed in practice; i.e., perpendicular laser beam impingement on a work piece surface and angled TIG welding torch with a small lateral offset in position. The arc continuity equations were solved, including a term $\kappa_\omega S$ for the laser irradiation in the energy balance equation, where κ_ω is the inverse Bremsstrahlung coefficient and S is the time averaged beam energy density determined from the complex amplitude of the electric field of the beam in the absence of the plasma A_ω viz:

$$-2ik\frac{\partial A_\omega}{\partial z} = \frac{1}{r}\frac{\partial}{\partial r}\left(r\frac{\partial A_\omega}{\partial r}\right) + k^2(\varepsilon_\omega - 1)A_\omega. \tag{7.80}$$

Here k is the wave vector, and ε_ω is the relative complex dielectric permittivity of the plasma at a radiation frequency of ω. The beam energy density [W m^{-2}] is given by

$$S = \frac{1}{2}\left(\frac{\varepsilon_0}{\mu_0}\right)|A_\omega|^2. \tag{7.81}$$

For a 150 A TIG arc, absorption results in an increase in axial plasma temperatures of about 4,000 K and 13,000 K for CO_2 laser beam powers of 500 W and 1500 W respectively. The axial temperatures were increased throughout the arc, however substantial radial differences were limited to radii of less than about 1 mm, governed by the laser beam profile. Laser absorption resulted in a 50% increase in current density at the anode for a 500 W beam and more than 150% increase for the 1500 W beam, with corresponding increase in axial energy density at the anode surface.

A number of works consider the influence of laser-arc hybrid welding on various aspects of the resultant weld. For example, Piekarska et al. [105] address phase transformations in a butt-welded structural steel, taking account of the fluid flow in the weld pool and accounting for latent heat due to solid phase changes as well as state changes. The kinetics of phase transformations were calculated on the basis of the Johnson–Mehl-Avrami (JMA) model and the volumetric fractions of phases from the Koistinen-Marburger (KM) equation. The trailing conduction mode laser component acted mainly to increase material penetration depth, as evidenced by a modified velocity distribution in the weld pool. Predictions of martensite phase fractions showed reasonable agreement with the measured phase profile of the welded joint. Cho et al. [106] simulated the weld bead shape and alloying element distribution in CO_2 laser–GMA hybrid welding of a structural steel with a stainless steel consumable. In this case a laser-keyhole condition was described with a laser-leading configuration. The model successfully describes the irregular partial penetration bead profile, attributed to a clockwise-rotating vortex with alternating high and low alloying element content resulting in a region of imperfect mixing.

Again predicted and experimental results show good first order agreement. Output from these models, [105, 106] together with a number of others [107–109], describe various aspects of the dynamic flow development in the weld pool and (where applicable) in the keyhole. These numerical approaches are based on summing the heat source terms separately, without accounting for the changes in arc and laser beam power density distributions due to mutual interactions. Nevertheless, despite the inevitable assumptions required to maintain numerical tractability, the results show good first order agreement with experimental observations, indicating that for prediction purposes, such an approach can often be appropriate.

References

1. Guile AE (1969) Arc cathode and anode phenomena. International Institute of Welding (IIW) Document 212-170-69
2. Lancaster J (1984) The physics of welding. Pergamon Press
3. Ducharme R, Kapadia P, Dowden J, Thornton M, Richardson IM (1995) A mathematical model of the arc in electric arc welding, including shielding gas flow and cathode spot location. J Phys D Appl Phys 28(9):1840–1850
4. Kovitya P, Lowke JJ (1985) Two-dimensional analysis of free burning arcs in argon. J Phys D Appl Phys 18:53–70
5. Haddad GN, Farmer AJD (1984) Temperature determinations in a free-burning arc: I. Experimental techniques and results in argon. J Phys D Appl Phys 17:1189–1196
6. Olsen HN (1959) Thermal and electrical properties of an argon plasma. Phys Fluids 2 (6):614–623
7. Greim HR (1964) Plasma spectroscopy. McGraw-Hill
8. Degout D, Catherinot A (1986) Spectroscopic analysis of the plasma created by a double-flux tungsten inert-gas (TIG) arc plasma torch. J Phys D Appl Phys 19(5):811–823
9. Thornton MF (1993) Spectroscopic determination of temperature distributions for a TIG Arc. PhD thesis, Cranfield Institute of Technology, UK
10. Cram LE, Poladian L, Roumeliotis G (1988) Departures from equilibrium in a free-burning argon arc. J Phys D: Appl Phys 21:418–425
11. Gomés AM (1983) Criteria for partial LTE in an argon thermal discharge at atmospheric pressure; validity of the spectroscopically measured electronic temperature. J Phys D Appl Phys 16:357–378
12. Drellischak KS, Knopp CF, Cambel AB (1962) Partition functions and thermodynamic properties of argon plasma. Gas Dynamics Laboratory, Nothwestern University, Illinois, USA. Report No A-3-62
13. Farmer AJD, Haddad GN (1988) Rayleigh-scattering measurements in a free-burning argon arc. J Phys D Appl Phys 21(3):426–431
14. Farmer AJD, Haddad GN (1984) Local thermodynamic-equilibrium in free-burning arcs in argon. Appl Phys Lett 45(1):24–25
15. Bakshi V, Kearney RJ (1989) An investigation of local thermodynamic equilibrium in an argon plasma jet at atmospheric pressure. J Quant Spect Rad Trans 41(5):369–376
16. Snyder SC, Lassahn GD, Reynolds LD (1993) Direct evidence of departures from local thermal equilibrium in a free-burning arc-discharge plasma. Phys Rev E 48(5):4124–4127
17. Kitamura T, Takeda K, Shibata K (1998) Deviation from local thermal equilibrium state in thermal plasma. ISIJ Int 38(11):1165–1169
18. Thornton MF (1993) Spectroscopic determination of temperature distributions for a TIG Arc. J Phys D Appl Phys 26:1432–1438

19. Rat V, Aubreton J, Elchinger MF, Fauchais P, Murphy AB (2002) Diffusion in two-temperature thermal plasmas. Phys Rev E 66:056407

20. Murphy AB (1996) Modelling and diagnostics of plasma chemical processes in mixed-gas arcs. Pure Appl Chem 68(5):1137–1142

21. Murphy AB (1993) Diffusion in equilibrium mixtures of ionized gases. Phys Rev E 44 (5):3594–3603

22. Murphy AB (1996) A comparison of treatments of diffusion in thermal plasmas. J Phys D Appl Phys 29(7):1922–1932

23. Murphy AB, Arundell CJ (1994) Transport coefficients of argon, nitrogen, oxygen, argon-nitrogen, and argon-oxygen plasmas. Plasma Chem Plasma Process 14(4):451–490

24. Devoto RS (1966) Transport properties of ionized monatomic gases. Phys Fluids 9(6):1230–1240

25. Murphy AB (1996) The influence of demixing on the properties of a free burning arc. Appl Phys Lett 69(3):323–330

26. Murphy AB (1997) Demixing in free-burning Arcs. Phys Rev E 55(6):7473–7494

27. Greses-Juan J (1999) Examination of adaptive control strategies for hyperbaric keyhole plasma arc welding. MSc thesis, Cranfield University, UK

28. Aubreton A, Elchinger MF (2003) Transport properties in non-equilibrium argon, copper and argon–copper thermal plasmas. J Phys D Appl Phys 36(15):1798–1805

29. Rethfeld B, Wendelstorf J, Klein T, Simon G (1996) A Self-consistent model for the cathode fall region of an electric arc. J Phys D Appl Phys 29:121–128

30. Chen MM, Thorne RE, Wyner EF (1976) Resolution of electron emission mechanisms in an argon arc with hot tungsten cathode. J Appl Phys 47(12):5214–5217

31. Klein T, Paulini J, Simon G (1994) Time-resolved description of cathode spot development in vacuum arcs. J Phys D Appl Phys 27:1914–1921

32. Morrow R, Lowke JJ (1993) A one-dimensional theory for the electrode sheaths of electric-arcs. J Phys D Appl Phys 26(4):634–642

33. Spataru C, Teillet-Billy D, Gauyacq JP, Teste P, Chabrerie JP (1997) Ion-assisted electron emission from a cathode in an electric arc. J Phys D Appl Phys 30:1135–1145

34. Hsu KC, Pfender E (1983) Analysis of the cathode region of a free burning high intensity argon arc. J Appl Phys 54(7):3818–3824

35. Delalondre C, Simonin O (1990) Modeling of high-intensity arcs including a non-equilibrium description of the cathode sheath. J De Phys 51(18):C5199–C5206

36. Wendelstorf J (2000) Ab initio modelling of thermal plasma gas discharges (electric arcs). PhD thesis, University of Braunschweig, Germany

37. Murphy EL, Good RH (1956) Thermionic emission, field emission and the transition region. Phys Rev 102(6):1464–1473

38. Coulombe S, Meunier JL (1997) A comparison of electron-emission equations used in arc-cathode interaction calculations. J Phys D Appl Phys 20(30):2905–2910

39. Quigley MBC, Richards PH, Swift-Hook DT, Gick AEF (1973) Heat-flow to the workpiece from a TIG welding arc. J Phys D Appl Phys 6(18):2250–2258

40. Ushio M, Tanaka M, Lowke JJ (2004) Anode melting from free-burning argon arcs. IEEE Trans Plasma Sci 32(1):108–117

41. Tanaka M, Ushio M, Wu CS (1999) One-dimensional analysis of the anode boundary layer in free-burning argon arcs. J Phys D Appl Phys 32:605–611

42. Lowke JJ, Morrow R, Haidar J (1997) A simplified unified theory of arcs and their electrodes. J Phys D Appl Phys 30:2033–2042

43. Hinnov E, Hirschberg JG (1962) Electron-ion recombination in dense plasmas. Phys Rev 125(3):795–801

44. Jenista JJ, Heberlein VR (1997) Numerical model of the anode region of high current electric arcs. IEEE Trans Plasma Sci 25(5):883–890

45. Zhu P, Lowke JJ, Morrow R, Haider J (1995) Prediction of anode temperatures of free burning arcs. J Phys D Appl Phys 28:1369–1376

46. Sanders NA, Pfender E (1984) Measurement of anode falls and anode heat transfer in atmospheric pressure high intensity arcs. J Appl Phys 55(3):714–722
47. Yang G, Heberlein J (2007) Anode attachment modes and their formation in a high intensity argon arc. Plasma Sources Sci Technol 16:529–542
48. Kim W-H, Na S-J (1998) Heat and fluid flow in pulsed current GTA weld pool. Int J Heat and Mass Trans 41:3213–3227
49. Zhang W, Kim C-H, DebRoy T (2004) Heat and fluid flow in complex joints during gas metal arc welding part I: numerical model of fillet welding. J Appl Phys 95(9):5210–5219
50. Wu CS, Yan F (2004) Numerical simulation of transient development and diminution of weld pool in gas tungsten arc welding. Modell Simul Mater Sci Eng 12:13–20
51. Mishra S, DebRoy T (2005) A heat-transfer and fluid-flow based model to obtain a specific weld geometry using various combinations of welding variables. J Appl Phys 98:044902
52. Chakraborty N, Chakraborty S, Dutta P (2004) Three-dimensional modeling of turbulent weld pool convection in GTAW processes. Numer Heat Transf. A 45:391–413
53. Jaidi J, Dutta P (2004) Three-dimensional turbulent weld pool convection in gas metal arc welding process. Sci Technol Weld Join 9(5):407–414
54. Goodarzi M, Choo R, Toguri JM (1997) The effect of the cathode tip angle on the gas tungsten arc welding arc and weld pool: I. Mathematical model of the arc. J Phys D Appl Phys 30:2744–2756
55. Goodarzi M, Choo R, Takasu T, Toguri JM (1998) The effect of the cathode tip angle on the gas tungsten arc welding arc and weld pool: II. The mathematical model for the weld pool. J Phys D Appl Phys 31:569–583
56. Tanaka M, Ushio M, Lowke JJ (2004) Numerical study of gas tungsten arc plasma with anode melting. Vacuum 73:381–389
57. Tanaka M, Ushio M, Lowke JJ (2004) Numerical analysis for weld formation using a free-burning helium arc at atmospheric pressure. JSME Int J Series B 48(3):397–404
58. Lowke JJ, Tanaka M, Ushio M (2004) Mechanisms giving increased weld depth due to a flux. J Phys D: Appl Phys 38:3438–3445
59. Lowke JJ, Tanaka M (2007) Predictions of weld pool profiles using plasma physics. J Phys D: Appl Phys 40:R1–R23
60. Tanaka M, Tashiro S, Lowke JJ (2007) Predictions of weld formation using gas tungsten arcs for various arc lengths from unified arc-electrode model. Sci Technol Weld Join 12(1):2–9
61. Lago F, Gonzalez JJ, Freton P, Gleizes A (2004) A numerical modelling of an electric arc and its interaction with the anode: part I. The two-dimensional model. J Phys D Appl Phys 37:883–897
62. Gonzalez JJ, Lago F, Freton P, Masquère M, Franceries X (2005) Numerical modelling of an electric arc and its interaction with the anode: part II. The three-dimensional model—influence of external forces on the arc column. J Phys D: Appl Phys 38:306–318
63. Tanaka M, Yamamoto K, Tashiro S, Nakata K, Ushio M, Yamazaki K, Yamamoto E, Suzuki K, Murphy AB, Lowke JJ (2007) Metal vapour behaviour in thermal plasma of gas tungsten arcs during welding. International Institute of Welding (IIW) Document 212-1107-07
64. Hu J, Tsai HL (2007) Heat and mass transfer in gas metal arc welding. part I: the arc. Int J Heat Mass Trans 50:808–820
65. Hu J, Tsai HL (2007) Heat and mass transfer in gas metal arc welding. part II: the metal. Int J Heat Mass Trans 50:833–846
66. Hu J, Tsai HL (2006) Effects of current on droplet generation and arc plasma in gas metal arc welding. J Appl Phys 100:053304
67. Quinn TP, Szanto M, Gilad I, Shai I (2205) Coupled arc and droplet model of GMAW. Sci Technol Weld Join 10(1):113–119
68. Steen WM, Eboo M (1979) Arc Augmented Laser-Welding. Metal Construction 11(7):332–335

69. Steen WM, Eboo M, Clarke J (1978) Arc augmented laser welding. Proceedings 4th international conference advances in welding processes, Harrogate, UK, 9–11 May. Paper 17: 257–265
70. Deron C, Rivière P, Perrin M-Y, Soufiani A (2006) Coupled radiation, conduction, and joule heating in argon thermal plasmas. J Thermophys Heat Trans 20(2):211–219
71. Hughes TP (1975) Plasmas and laser light, Adam Hilger
72. Paulini J, Simon G (1993) A theoretical lower limit for laser power in laser-enhanced arc welding. J Phys D Appl Phys 26:1523–1527
73. Seyffarth P, Krivtsun IV (2002) Laser-arc processes and their applications in welding and material treatment. Weld Allied Process vol 1. Taylor & Francis
74. Wang T-S, Rhodes R (2003) Thermophysics characterization of multiply ionized air plasma absorption of laser radiation. J Thermophys Heat Trans 17(2):217–224
75. Stallcop JR, Billman KW (1974) Analytical formulae for the inverse bremsstrahlung absorption coefficient. Plasma Physics 16:1187–1189
76. Devoto RS (1973) Transport coefficients of ionised argon. Phys Fluids 16(5):616–623
77. Mathuthu M, Raseleka RM, Forbes A, West N (2006) Radial variation of refractive index, plasma frequency and phase velocity in laser induced air plasma. IEEE Trans Plasma Sci 34 (6):2554–2560
78. Howlader MK, Yang Y, Roth JR (2005) Time-resolved measurements of electron number density and collision frequency for a fluorescent lamp plasma using microwave diagnostics. IEEE Trans Plasma Sci 33(3):1093–1099
79. Lacroix D, Jeandel G, Boudot C (1998) Solution of the radiative transfer equation in an absorbing and scattering Nd:YAG laser-induced plume. J Appl Phys 84(5):2443–2449
80. Kokhanovsky AA (1999) Optics of light scattering media. Wiley and Praxis Publishing
81. Greses J (2003) Plasma/plume effects in CO_2 and Nd:YAG laser welding. PhD thesis, Cambridge University, UK
82. Greses J, Hilton PA, Barlow CY, Steen WM (2002) Plume attenuation under high power Nd: YAG laser welding. J Laser Appl 16(1):9–15
83. Zimmer AT, Biswas P (2001) Characterization of the aerosols resulting from arc welding processes. J Aerosol Science 32:993–1008
84. Hewett P (1995) The particle size distribution, density, and specific surface area of welding fumes from SMAW and GMAW mild and stainless steel consumables. American Industrial Hygiene Association, Journal 56:128–135
85. Thomas ME (2006) Optical propagation in linear media. Oxford University Press
86. Hansen F, Duley WW (1994) Attenuation of laser radiation by particles during laser materials processing. J Laser Appl 6(3):137–143
87. Tu J, Miyamoto I, Inoue T (2002) Characterizing keyhole plasma light emission and plasma plume scattering for monitoring 20 kW class CO_2 laser welding processes. J Laser Appl 14 (3):146–153
88. Kozakov R, Gott G, Uhrlandt D, Emde B, Hermsdorf J, Wesling V (2015) Study of laser radiation absorption in a TIG welding arc. Weld World 59(4):475–481
89. Kozakov R, Emde B, Pipa AV, Huse D, Uhrlandt D, Hermsdorf J, Wesling V (2015) Change of electrical conductivity of Ar welding arc under resonant absorption of laser radiation. J Phys D Appl Phys 48:095502
90. Miller R, DebRoy T (1990) Energy absorption by metal-vapour-dominated plasma during carbon dioxide laser welding of steels. J Appl Phys 68(5):2045–2050
91. Bagger C, Olsen F (2005) Review of laser hybrid welding. J Laser Appl 17(1):2–14
92. Chen Y, Li L, Fang J, Feng X, Wu L (2003) Temperature field simulation of laser-TIG hybrid welding. China Weld 12(1):62–66
93. Chen Y, Li L, Fang J, Feng X (2003) Numerical analysis of energy effect in laser-TIG hybrid welding. J Mater Sci Technol 19(Suppl 1):23–26
94. Hu B (2002) Nd:YAG laser-assisted arc welding. PhD thesis Delft University of Technology, The Netherlands

95. Reutzel EW, Kelly SM, Martukanitz RP, Bugarewicz MM and Michaleris P (2005) Laser-GMA [MIG/MAG] hybrid welding: process monitoring and thermal modelling. In: David SA, DebRoy T, Lippold JC, Smartt HB, Vitek JM (eds) Proceedings of the 7th international conference trends in welding research, pine mountain, GA, USA, 16–20 May 2005. Publ, Materials Park, OH 44073-0002, USA, ASM International, 2006, 143–148

96. Goldak J, Chakravarti A, Bibby M (1984) A new finite element model for welding heat sources. Met Trans B 15B:299–305

97. Zaĭkin AE, Katulin VA, Levin AV, Petrov AL (1991) Hydrodynamic processes in a melt bath under laser-arc interaction conditions. Sov J Quantum Electron. 21(6):635–639

98. Gratzke U, Kapadia PD, Dowden J (1991) Heat-conduction in high-speed laser-welding. J Phys D: Appl Phys 24(12):2125–2134

99. Cline HE, Anthony TR (1977) Heat treating and melting material with a scanning laser or electron-beam. J Appl Phys 8(9):3895–3900

100. Hu B, den Ouden G (2005) Synergic effects of hybrid laser/arc welding. Sci Technol Weld Join 10(4):427–431

101. Dowden J, Kapadia PD (1998) The use of a high power laser to provide an electrical path of low resistance. J Laser Appl 10(5):219–223

102. Startsev VN, Martynenko DP, Leonov AF (2000) Investigation of characteristics of an arc column in laser arc welding using numerical simulation. High Temp 38(1):24–29

103. Mahrle A, Rose S, Schnick M, Pinder T, Beyer E and Fussel U (2102) Improvements of the welding performance of plasma arcs by a superimposed fibre laser beam, Proc SPIE 8239 83290D-1:13

104. Reisgen U, Zabirov A, Krivtsun I, Demchenko V, Krikent I (2015) Interaction of CO_2-laser beam with argon plasma of Gs tungsten arc. Weld World 59(5):611–622

105. Piekarska W, Kubiak M, Bokota A (2011) Numerical simulation of thermal phenomena and phase transformations in laser-arc hybrid welded joints. Arch Metall Mater 56(2):409–421

106. Zhou J and Tsai HL (2012) In: Kovacevic R Hybrid laser-arc welding, in book "Welding Processes", ISBN 978-953-51-0854-2, pub In-Tech

107. Kong F, Ma J, Kovacevic R (2011) Numerical and experimental study of thermally induced residual stress in the hybrid laser–GMA welding process. J Mater Process Technol 211:1102–1111

108. Zhou J, Tsai HL (2012) Modeling of transport phenomena in hybrid laser-MIG keyhole welding. Int J Heat Mass Transfer 51:4353–4366

109. Le Guen E, Carin M, Fabbro R, Coste F, Le Masson P (2011) 3D heat transfer model of hybrid laser Nd:Yag-MAG welding of S355 steel and experimental validation. Int J Heat Mass Transfer 54:1313–1322

110. Zijp JP (1990) Heat transport during gas tungsten arc welding. PhD thesis, Delft University of Technology, The Netherlands